

UNIVERSITÄT TÜBINGEN

BACHELOR THESIS

---

# Exploring Time Variability Properties of X-ray Pulsars through Accretion Torque Models

---

Inga SAATHOFF

Hagstrasse 2

72762 Reutlingen

inga.saathoff@student.uni-tuebingen.de

Supervisors:

Prof. Dott. Andrea SANTANGELO

Dr. Lorenzo DUCCI

April 2019



## Eidesstattliche Erklärung

Hiermit erkläre ich, Inga SAATHOFF, dass ich die vorliegende Bachelorarbeit mit dem Titel “Exploring Time Variability Properties of X-ray Pulsars through Accretion Torque Models” selbstständig verfasst und dabei keine anderen als die angegebenen Quellen und Hilfsmittel benutzt habe.

---

Ort, Datum

---

Unterschrift



---

# Abstract

---

In this thesis, accretion torque models for accreting pulsars in X-ray binaries are investigated. The inclined rotator model by Perna et al. (2006) is studied and a time variability of the mass supply rate from the companion  $\dot{M}_*$  is introduced to the model, in order to achieve a superposition of a long-term spin-up or spin-down trend on short-term spin-up/spin-down reversals. The model is then applied to the pulsar in OAO 1657-415 and a magnetic field strength of  $7 \times 10^{13}$  G is determined.

In a second part of the work, data from *Fermi*/GBM and *Swift*/BAT is used to study the torque-flux relation of OAO 1657-415, using accretion torque models by Ghosh & Lamb (1978, 1979a,b), Wang (1987) and Wang (1995). During the spin-up phases, matter is likely accreted from a stable accretion disk, whereas the accretion processes during spin-down of the pulsar remain elusive. Some possibilities explaining the observations, such as accretion from a retrograde disk or sub-Keplerian behavior of the disk, are discussed. The domain in-between the two branches, where the torque is small, shows a highly scattered flux. The accretion-torque models by Ghosh & Lamb (1979b); Wang (1987, 1995) are applied to the data from the spin-up branch to constrain the magnetic field of the pulsar in OAO 1657-415 between about  $2 \times 10^{10}$  G to  $2 \times 10^{12}$  G and its distance between approximately 8 kpc to 15 kpc.



---

# Contents

---

<b>List of Figures</b>	<b>ix</b>
<b>List of Tables</b>	<b>xi</b>
<b>1 Introduction</b>	<b>1</b>
1.1 Units . . . . .	3
1.2 Nomenclature . . . . .	3
<b>2 Astrophysical Background</b>	<b>5</b>
2.1 X-ray Binaries . . . . .	5
2.1.1 Accretion Processes . . . . .	5
2.1.2 Classification . . . . .	7
2.2 Sources and Observations . . . . .	8
2.2.1 Observational Properties . . . . .	8
2.2.2 Sources . . . . .	9
<b>3 Accretion-Torque Models</b>	<b>15</b>
3.1 Accretion on Magnetized Objects . . . . .	15
3.2 Magnetic Coupling between the Star and Disk . . . . .	17
3.2.1 The Basic Model by Ghosh & Lamb . . . . .	17
3.2.2 An Improved Accretion-Disk Torque . . . . .	19
3.2.3 The Retrograde Disk Model . . . . .	20
3.2.4 The Sub-Keplerian Disk Model . . . . .	21
3.3 The Inclined Rotator Model . . . . .	23
<b>4 Applying an Inclined Accretion Torque Model to OAO 1657-415</b>	<b>31</b>
4.1 Exploration of the Model . . . . .	31
4.2 Introducing a Time Variable $\dot{M}_*$ . . . . .	35
4.3 The Spin-Period Evolution of OAO 1657-415 . . . . .	36
<b>5 Torque-Flux Correlation of OAO 1657-415</b>	<b>39</b>
5.1 Data Processing . . . . .	40
5.1.1 <i>Fermi</i> /GBM . . . . .	40
5.1.2 <i>Swift</i> /BAT . . . . .	41
5.2 Torque-Flux Correlation . . . . .	45
5.2.1 Correlation Coefficient and Probability . . . . .	45
5.2.2 Applying Accretion-Torque Models . . . . .	46
5.2.3 Calculating the Magnetic Field of OAO 1657-415 . . . . .	51
5.2.4 Distance Determination . . . . .	52
5.2.5 Simultaneous Calculation of Magnetic Field and Distance . . . . .	55

<b>6 Conclusion</b>	<b>57</b>
<b>Bibliography</b>	<b>59</b>



---

# List of Figures

---

1.1	Illustration of an accreting pulsar. . . . .	2
2.1	Illustration of accretion mechanisms. . . . .	6
2.2	Equipotential surfaces in a binary system. . . . .	6
2.3	Illustration of a BeXRB . . . . .	8
2.4	Long-term frequency histories. . . . .	10
2.5	Period history of OAO 1657-415. . . . .	11
2.6	Frequency history of GX 1+4. . . . .	12
2.7	Frequency history of 4U 1626-67. . . . .	13
3.1	Transition zone in the GL model. . . . .	17
3.2	Spin-up rate over $PL^{3/7}$ . . . . .	18
3.3	Spin-up and spin-down transitions in the GL model. . . . .	20
3.4	Torque reversals of three pulsars. . . . .	21
3.5	Schematic representation of the aligned and misaligned NS system. . .	23
3.6	Schematic illustration of the oblique NS rotator. . . . .	24
3.7	Mass flow rate components. . . . .	25
3.8	Contributions to the total mass flow rate $\dot{M}_{\text{tot}}$ . . . . .	26
3.9	Hysteresis limit cycles. . . . .	27
3.10	Time evolution. . . . .	28
3.11	Results found with the PBS model for GX 1+4 and 4U 1626-67. . . . .	29
4.1	Comparison of the frequency, frequency derivative and luminosity his- tories of different parameters. . . . .	32
4.2	Comparison of the frequency, frequency derivative and luminosity his- tories of different parameters. . . . .	34
4.3	Time variable $\dot{M}_*$ from the companion star. . . . .	36
4.4	Possible solution for OAO 1657-415. . . . .	37
5.1	Frequency history, frequency derivative and BAT flux as presented by Jenke et al. (2012). . . . .	39
5.2	Torque-flux relation of the pulsar in OAO 1657-415 (Jenke et al. 2012). .	40
5.3	Frequency, frequency derivative, BAT Flux and root mean square (rms) of OAO 1657-415 from MJD 54694 to 58460. . . . .	42
5.4	Orbital phase diagrams of OAO 1657-415. . . . .	44
5.5	BAT flux, residuals and rms over $\dot{\nu}$ . . . . .	48
5.6	BAT flux, residuals and rms over $\dot{\nu}$ . . . . .	49
5.7	Root mean square (rms) histograms. . . . .	51
5.8	Calculating the magnetic field and distance of OAO 1657-415 using different models. . . . .	53



---

# List of Tables

---

2.1	Source parameters. . . . .	9
3.1	Results for three pulsars from Yi et al. (1997a,b). . . . .	22
3.2	PBS results for GX 1+4 and 4U 1626-67. . . . .	29
4.1	Estimates of the equilibrium frequency, amplitude and timescale of variability for two magnetic field strengths. . . . .	33
4.2	Equilibrium frequency, amplitude and timescale of variability for two magnetic field strengths. . . . .	33
5.1	Best fit parameters for a spectral model of OAO 1657-415 (Orlandini et al. 1999). . . . .	43
5.2	Correlation coefficient and probability for the torque-flux data. . . . .	46
5.3	Determined constants $C_1$ , $C_2$ , $D$ and residual variance from the fitted $\dot{\nu}$ -flux data. . . . .	47
5.4	Literature values of the magnetic field strength of OAO 1657-415. . . . .	52
5.5	Distance and magnetic field strength calculated using different models. . . . .	54
5.6	Literature values of the distance to OAO 1657.415. . . . .	55



# Introduction

---

At the end of stellar evolution, the core of a star runs out of nuclear fuel and collapses. In neutron stars this collapse is stopped by the so-called neutron degeneracy pressure. This pressure arises because neutrons are fermions and are therefore subject to the Pauli exclusion principle, which states that identical fermions cannot occupy the same quantum state simultaneously (Longair 2011). Neutron stars are compact objects, with typical masses of about  $1.4 M_{\odot}$  and radii of  $\sim 12$  km, which corresponds to a density of about  $10^{14} \text{ g cm}^{-3}$ , and magnetic field strengths of approximately  $10^8$  to  $10^{13}$  G. These extreme conditions make neutron stars especially interesting as they offer unique laboratories that cannot be matched on Earth.

These extreme objects are observed in a wide variety of systems and environments. They can exist isolated or in binary systems, for example with other stars, white dwarfs, neutron stars or black holes. For some, regular light pulses can be detected and these neutron stars are therefore called “pulsars”. Others show sudden one-off or recurring bursts on time scales of seconds, or outbursts on time scales of days to years. This thesis studies accreting X-ray binaries (XRBs). These systems contain a neutron star, which accretes matter from a companion star. The X-ray energy range, which spans from about 0.1 keV to several hundreds of keV, is of particular importance in this context, because it is in this range that most of the luminosity of XRBs is emitted from the surface of the neutron star and the matter in its immediate vicinity.

The first pulsar was discovered in 1971 with the Uhuru satellite (Giacconi et al. 1971). The nature of the observed source Centaurus X-3 (Cen X-3) was determined solely by these observations. The detected X-ray pulsations with a period of 4.84 s can only be caused by a rotating neutron star, because a white dwarf could not rotate with this frequency without being torn apart by centrifugal force. A variation of the pulse period every 2.09 d suggested that it is a binary system, with the neutron star orbiting a companion star. During this binary orbit, the X-ray signal disappears completely for about 11 h, so that it must be an eclipsing XRB (Seward & Charles 2010).

The principle of X-ray pulsars was quickly understood: a rotating and strongly magnetized neutron star accretes matter from a stellar companion, possibly through an accretion disk. When this plasma approaches the compact object, it is guided to the magnetic poles by the strong magnetic field. At the poles, the gravitational energy is converted into a beam of X-rays and  $\gamma$ -rays (Bildsten et al. 1997). As illustrated in Figure 1.1, the pulsations are observed because the neutron star is rotating, its magnetic and rotational axes are misaligned, and the observed beam is in line of sight with the Earth.

As more X-ray pulsars were discovered and studied, a wide range of different properties was revealed. For example, the frequency of some sources increased (decreased) over time, which is called a spin-up (spin-down), sometimes with (or without) simultaneous changes in their luminosity. To explain these observations, simplified physical models of the neutron star with its magnetic field were developed and studied with

respect to their frequencies and luminosities. In the present work, one source in particular was studied using some of these models. OAO 1657-415 was first detected by the Copernicus satellite in 1978 and HEAO-1 later determined a pulse period of  $\sim 38.22$  s. It is a high mass XRB with a  $\sim 10.4$  d binary orbit found in the constellation Scorpius at a distance of about 7.1 kpc. The mass of the neutron star is  $\sim 1.74 M_{\odot}$  and its companion star is an Ofpe/WN9 star, which is an object between OB main sequence stars and hydrogen depleted Wolf-Rayet stars, with a mass of about  $17.5 M_{\odot}$  (Mason et al. 2009, 2012; Falanga et al. 2015). This source is of special interest because it showed several transitions from spin-up and spin-down on short timescales in the past, with on an overall long-term spin-up trend. Due to its highly dynamic behavior, the system has so far been elusive.

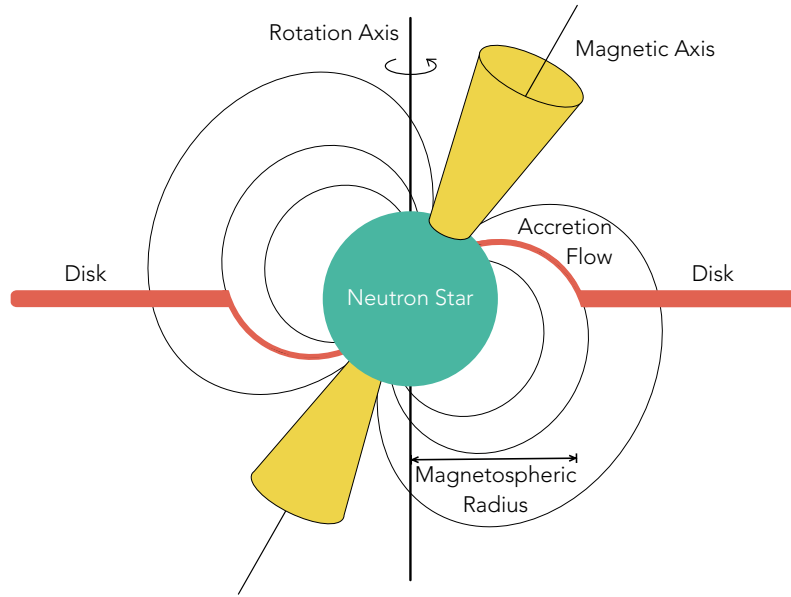


Figure 1.1: Illustration of an accreting pulsar. Matter that is gravitationally captured by a neutron star from a companion can form an accretion disk. As the matter approaches the neutron star, it is then channeled via the magnetic field lines to the magnetic poles of the neutron star. At the poles it can release its gravitational energy and emit thermal radiation in directional beams.

According to a study by Perna et al. (2006), a cyclic spin-up/spin-down behavior might be explained with an inclined rotator model, in which the rotation and magnetic axis are misaligned. The first aim of this thesis is to apply this model to OAO 1657-415. The model will then be further investigated and a new time-dependent component introduced to obtain a long-term spin-up or spin-down pattern that is superposed on the cyclic spin-up/spin-down reversals.

The second aim of this thesis is to examine the frequency history of OAO 1657-415 from over 10 years of data. The torque-flux relation is studied with *Fermi*/GBM as well as *Swift*/BAT data. In a third aim, the magnetic field strength and distance of OAO 1657-415 is determined comparing several different models (Ghosh & Lamb 1978, 1979a,b; Wang 1987, 1995).

In the following Section 1.1, an overview of the units used in this work is given, followed by an introduction to the pulsar nomenclature in Section 1.2. Chapter 2 presents

the general astrophysical background, including an introduction to X-ray binary systems in Section 2.1, their classification and accretion processes, and an overview of their observational properties and the sources studied in Section 2.2. Chapter 3 presents some of the models to explain the observed properties, starting with the general picture of the accretion on magnetized objects in Section 3.1, followed by models with the magnetic coupling between star and disk in Section 3.2 and finally a model that takes into account the inclination between rotation and magnetic axis in Section 3.3. Chapter 4 includes the analysis and investigation of the inclined rotator model and the pulse timing analysis of the source OAO 1657-415 is shown in Chapter 5. Chapter 6 briefly summarizes the results.

This thesis implements the spirit of Reproducible Research. Clearbout (1990) proposed that everything necessary to reproduce the results of a work should be available. This includes programs and data files. Therefore, the key program (written in Python) for reproducing the results of Chapter 4 is available under <https://gitlab.com/isaathoff/inclined-rotator>.

## 1.1 Units

In this thesis, physical quantities are given in the centimeter-gram-second (cgs) system of units, which is common to astrophysics, with a few exceptions. Photon energies are given in keV, where  $1 \text{ keV} \approx 1.6 \times 10^{-9} \text{ erg}$ . Thus the X-ray waveband refers to an energy range of about 0.1 to 100 keV (Longair 2011). Distances to sources are stated in kpc with  $1 \text{ kpc} \approx 3.1 \times 10^{21} \text{ cm}$ . Masses and radii are indicated in solar masses ( $M_{\odot}$ ) and solar radii ( $R_{\odot}$ ) respectively, where  $1 M_{\odot} \approx 1.99 \times 10^{33} \text{ g}$  and  $1 R_{\odot} \approx 6.96 \times 10^{10} \text{ cm}$ . Notations such as  $\mu_{30}$  or  $\dot{M}_{17}$  denote the order of magnitude of the corresponding quantity, thus  $\mu_{30}$  is in units  $10^{30} \text{ G cm}^3$  and  $\dot{M}_{17}$  is in units  $10^{17} \text{ g s}^{-1}$ . Dates are given in the Modified Julian date (MJD) system, based on the Julian date (JD), which is an integer counter of the days beginning with 0 at noon, January 1, 4713 B.C. in Greenwich. MJD modifies the JD system by beginning count at midnight instead of noon and removing the first two digits, thus the conversion is  $\text{MJD} = \text{JD} - 2400000.5$ .

## 1.2 Nomenclature

X-ray source nomenclature has changed over time and the oldest sources were named according to the nearest constellation, for example Centaurus X-3 (Cen X-3). Newer sources are designated by their celestial coordinates: Sources in the galactic plane are signified by their galactic longitude and latitude, such as GX 1+4 which lies near  $l \approx 1^{\circ}$  and  $b \approx +4^{\circ}$ . More recent and accurate measurements determine the source to be at  $l = 1.937^{\circ}$  and  $b = +4.795^{\circ}$ . Other sources are known by a prefix indicating the satellite which discovered the source followed by their right ascension ( $\alpha$ ) and declination ( $\delta$ ), for example OAO 1657-415, which was discovered by the Copernicus Orbiting Astronomical Observatory 3 (OAO) satellite and lies near  $\alpha \approx 16^{\text{h}} 57^{\text{m}}$ ,  $\delta \approx -41^{\circ} 5'$ . The position of this source was later also more accurately determined to be at  $\alpha = 16^{\text{h}} 57^{\text{m}} 17.819^{\text{s}}$  and  $\delta = -41^{\circ} 34' 57.99''$ .





# Astrophysical Background

---

## 2.1 X-ray Binaries

X-ray binaries (XRBs) are star systems consisting of a compact object and a companion star. The compact object can be a white dwarf, a neutron star (NS) or a black hole, whereas the companion star is typically a main sequence star, an evolved star and, in some cases, a white dwarf. Due to their close proximity, matter can flow from the companion star (also called the donor or normal star) to the compact object (also called the accretor) in a process that is called accretion. When the accreted matter reaches the surface of the compact object, it can release its gravitational energy in the X-ray energy range, which extends from about 0.1 keV to a few hundred keV (Bradt 2008; Longair 2011). The most important accretion processes and mechanisms are reviewed in Section 2.1.1. In Section 2.1.2 the classification of XRBs by the mass of the companion star is explained.

### 2.1.1 Accretion Processes

There are two main mechanisms how matter is accreted from the companion star to the NS. As illustrated in Figure 2.1 and explained in the following, the two most important processes are Roche lobe overflow and wind accretion.

#### Roché Lobe Overflow

To understand the evolution of a binary star system, it is useful to look at its equipotential surfaces. In the rotating frame of reference of a binary star system, the stars possess a gravitational potential and an extra term is added to account for the centrifugal potential of motion. If  $r_1, r_2$  are the distances of the stars with mass  $M_1, M_2$  to a point  $r$ , then the equipotential surfaces are defined as

$$\phi = \frac{GM_1}{r_1} + \frac{GM_2}{r_2} - \Omega^2 r^2 = \text{const.}, \quad (2.1)$$

where  $\Omega$  is the angular velocity of the system (Longair 2011). Close to the stars, the equipotential surfaces are spherical. They increase in size and start to deform as they approach a saddle point, also called the inner Lagrangian point  $L_1$ , see Figure 2.2. The smallest equipotential surface that is common to both stars is called the Roche lobe. If a star takes up a significant part of the Roche lobe, for example when expanding during the course of evolution, its shape will be deformed to fill this surface and matter can be transferred through the Lagrangian point  $L_1$  toward the other star, see also Figure 2.1 a). The transferred matter is captured by the compact object and due to the conservation of angular momentum, an accretion disk can form around it (Shapiro & Teukolsky 1983; Longair 2011).

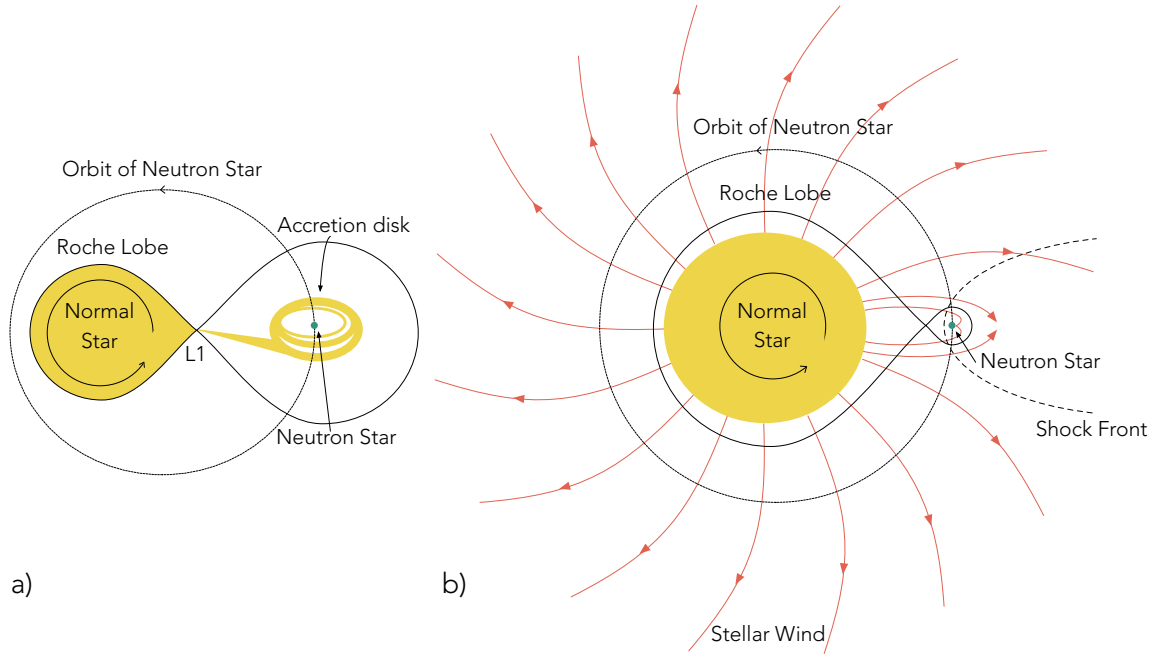


Figure 2.1: Illustration of accretion geometries. a) The normal (donor) star expands and fills its Roche lobe, matter can then pass through the Lagrangian point  $L_1$  to the NS. b) The normal star has a strong stellar wind from which the NS is accreting. Adapted from Shapiro & Teukolsky (1983).

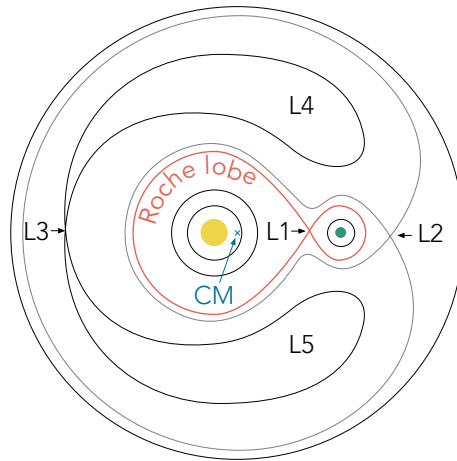


Figure 2.2: Schematic representation of equipotential surfaces in a binary system with different masses. The surfaces are spherically symmetric in close proximity of each star as well as at a large distance around the center of mass (CM). Between these limits they are deformed, the smallest common envelope is called the Roche lobe. There are five equilibrium points labeled  $L_1 - L_5$  called Lagrangian points.

## Wind accretion

When the Roche lobe is under-filled, accretion can only take place from winds. Strong stellar winds are observed in luminous O and B class stars. The compact object is embedded in this outflow, as illustrated in Figure 2.1 b). A mere fraction, less than 0.1%, of the ejected plasma can be captured by the compact star and accreted. A shock front forms and accretion can only take place within its cavity. Therefore accretion is mostly assumed to be spherical (Shapiro & Teukolsky 1983; Longair 2011) but an accretion disk may form if the infalling matter has sufficient angular momentum.

### 2.1.2 Classification

XRBs are typically classified into two categories, based on the mass of the companion from which they accrete matter.

#### High Mass X-ray Binaries

High Mass X-ray Binaries (HMXBs) are systems with a massive (greater than 6 to 7  $M_{\odot}$ ) companion star of OB type. These stars are very luminous but have short lifetimes on the main sequence of order  $10^7$  years (Longair 2011). This implies an age of the HMXBs smaller than a few tens of Myrs. Their orbital periods range from 0.2 days to a few years and the spin periods of the compact objects from 69 ms to about 14 ks. The magnetic fields in these systems have to be strong enough to channel the accreted matter to the NS's magnetic poles, causing beamed X-ray emission (see also Figure 1.1). This implies magnetic field strengths of about  $10^{11}$  to  $10^{13}$  G. The observed X-ray luminosities span a wide range, from  $10^{32}$  to  $10^{39}$  erg s $^{-1}$  (Revnivtsev & Mereghetti 2015; Reig 2011).

NSs with a Be type companion are called BeXRBs and they make up the largest population of HMXBs. A Be type star is a star of class B that additionally shows emission (e) lines in the optical/UV band. These emission lines indicate an extended disk of dense gas around the star from which the lines originate (Hanslmeier 2013). The formation mechanism of these disks is still poorly understood (Rivinius 2013; Reig 2011). BeXRBs are typically transient systems because of the variability of the size of the circumstellar disk and their geometric configuration, see Figure 2.3. They typically have moderately eccentric orbits ( $e \gtrsim 0.3$ ) and the NS passes close to or through the disk during periastron. Some of the matter can then be accreted from the disk. Roche lobe overflow can also occur during periastron passage or during giant X-ray outbursts. These outbursts occur when a large fraction of the circumstellar disk is thought to be accreted (Reig 2011; Revnivtsev & Mereghetti 2015).

In most cases, HMXBs accrete matter from a stellar wind, as explained in Section 2.1.1. If the accreted matter has sufficient angular momentum, an accretion disk may form, otherwise accretion takes place spherically. The strong magnetic fields in HMXBs cause the matter to be accreted in a channel forming an accretion column (Basko & Sunyaev 1976). Their spectra generally differ from a blackbody shape and are better described by a power law with an exponential high-energy cutoff (Revnivtsev & Mereghetti 2015).

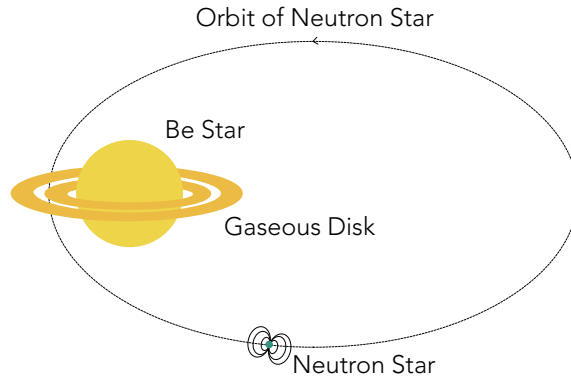


Figure 2.3: Illustration of a BeXRB. The NS is on an eccentric orbit around the Be star and passes its expelled disk only during periastron. Adapted from Kretschmar (1996).

### Low Mass X-ray Binaries

Low Mass X-ray Binaries (LMXBs) typically consist of a compact object and a companion of spectral class A to M with masses below  $1\text{--}2\,M_{\odot}$ . The dominant accretion mechanism in LMXBs is Roche lobe overflow, see Section 2.1.1. Their orbital periods are, with less than one day, generally much shorter than those of HMXBs. The presence of low mass stars indicate that LMXBs are much older systems, with ages up to a few Gyrs (Revnivtsev & Mereghetti 2015).

Most NSs in LMXBs are not detected as pulsars, since their magnetic fields below  $10^9\text{ G}$  are too weak to significantly affect the accretion flow (Bildsten et al. 1997). The low magnetic fields in LMXBs can be explained by the old age of the systems, as they will dispel over time. Those pulsars that have been detected in LMXBs, however, show spin periods that are much shorter than those in HMXBs (Revnivtsev & Mereghetti 2015).

## 2.2 Sources and Observations

### 2.2.1 Observational Properties

The main properties and characteristics of pulsars can be derived from frequency and flux observations. Figure 2.4 shows long-term frequency histories of several pulsars and a wide variety of behaviors can be seen. In the past, it has been believed that pulsars mostly show a steady increase of their pulse period (see Shapiro & Teukolsky 1983). This can be explained by the accretion of angular momentum. A rotating accretion disk may form because angular momentum is conserved. This disk is coupled to the NS via the magnetic field lines and this coupling can transfer the angular momentum from the disk to the star. Thus, when matter is accreted, so is angular momentum and the NS experiences a spin-up torque (Revnivtsev & Mereghetti 2015).

The long-term frequency histories seen in Figure 2.4, however, show more complex patterns. Her X-1, as seen in Figure 2.4a, displayed a long-term increase in frequency early on, followed by a long-term near equilibrium time with short-term spin-up/spin-down fluctuations. Vela X-1 shows similar fluctuations in Figure 2.4b with a longer spin-down trend in the course of observations. The frequency history of Cen X-3 shows

short-term fluctuations superposed on a long-term spin-up trend, see Figure 2.4c and 4U 1538 displays in Figure 2.4d mostly a long-term spin-down trend. The frequency histories of GX 1+4, 4U 1626-67 and OAO 1657-415 are shown in the following Section 2.2.2. In Chapter 3, different models to explain the observed properties will be introduced.

### 2.2.2 Sources

In this thesis, three accreting XRBs will be described and studied with regard to their time variability properties, with a special focus on OAO 1657-415. The other sources mentioned are GX 1+4 and 4U 1626-67. The location and type of these XRBs are listed in Table 2.1.

Table 2.1: Parameters of the studied sources. Locations are based on the International Celestial Reference System (ICRS), epoch J2000. Right ascension ( $\alpha$ ) is given in hours, minutes and seconds, declination ( $\delta$ ) in degrees, minutes and seconds.

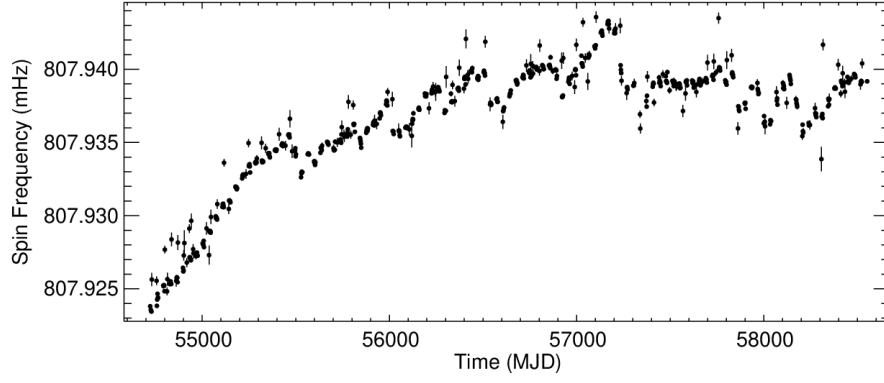
Object	$\alpha$	$\delta$	Type
OA0 1657-415	17 00 48.88	-41 39 21.46	HMXB
GX 1+4	17 32 02.15	-24 44 44.13	LMXB
4U 1626-67	16 32 16.79	-67 27 39.3	LMXB

#### OA0 1657-415

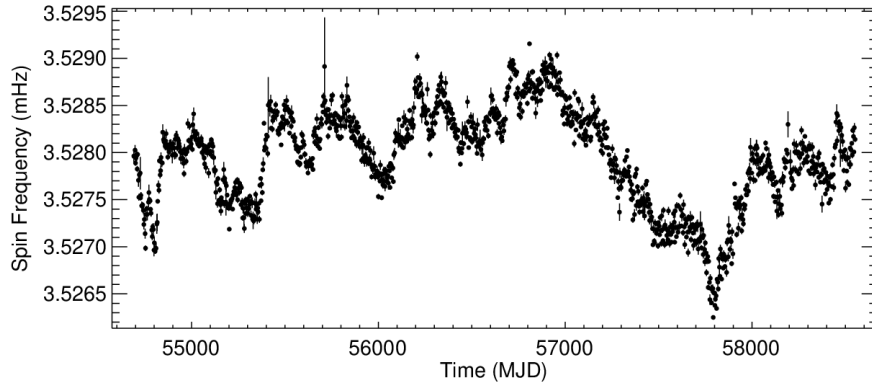
OA0 1657-415 was discovered by Copernicus, the Orbiting Astronomical Observatory 3 (OA0-3) in 1978 (Polidan et al. 1978) in the constellation Scorpius (Sco), the exact location can be found in Table 2.1. A follow-up observation by the High Energy Astronomy Observatory 1 (HEAO-1) detected 38.22 s pulsations from the source (White & Pravdo 1979). Spectroscopic observations showed a typical X-ray pulsar spectrum including a power law with a high energy cutoff. An iron line was also observed in the spectrum at 6.6 keV (Audley et al. 2006). In 1993, Chakrabarty et al. (1993) first determined that OA0 1657-415 is a HMXB, proposing that the companion is a supergiant of spectral class B0-B6 and thus implying a minimal distance of 11 kpc. The mass and radius of the companion was constrained to be 14 to 18  $M_{\odot}$  and 25 to 32  $R_{\odot}$  respectively. The first identification of the companion was done in infrared, confirming that the companion might be a highly-reddened B supergiant and allowing for a more precise distance estimation of  $(6.4 \pm 1.5)$  kpc (Chakrabarty et al. 2002). A more recent distance determination has been done by Audley et al. (2006), using the dust-scattered X-ray halo, a method proposed by Trümper & Schönfelder (1973). With this method, the distance was calculated to be approximately  $(7.1 \pm 1.3)$  kpc, consistent with the earlier estimate by Chakrabarty et al. (2002). Jenke et al. (2012) estimates the distance of the system to be between 3 kpc to 16 kpc, consistent with an earlier estimate by Mason et al. (2009) of 4.4 kpc to 12 kpc.

A spectral classification done by Mason et al. (2009) revealed that the companion star is most likely an Ofpe<sup>1</sup>/WNL star. This is a class of stars that is evolving from a

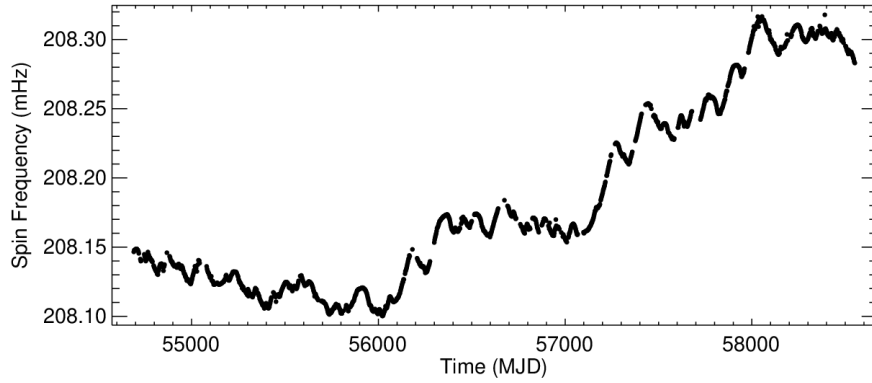
<sup>1</sup>Ofpe stars are stars with O-type spectra including hydrogen, helium and nitrogen emission lines, as well as other peculiarities.



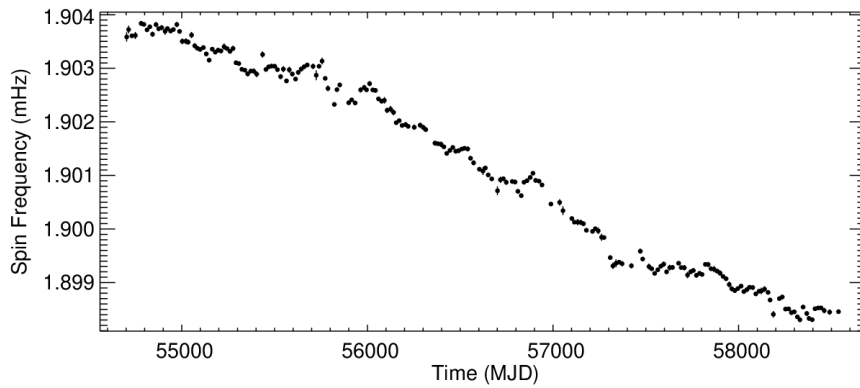
(a) Frequency history of Her X-1.



(b) Frequency history of Vela X-1.



(c) Frequency history of Cen X-3.



(d) Frequency history of 4U 1538.

Figure 2.4: Long-term frequency histories of the pulsars Her X-1, Vela X-1, Cen X-3 and 4U 1538 from the *Fermi*/GBM pulsar website (<https://gamma-ray.msfc.nasa.gov/gbm/science/pulsars.html>, accessed March 14, 2019).

massive O type star off the main sequence to Wolf-Rayet stars. Wolf-Rayet stars are hot stars that have lost most of their outer layers over time. WNL then describes late stage Wolf-Rayet stars whose spectra are dominated by nitrogen. The mass of the NS was calculated to be  $(1.42 \pm 0.26) M_{\odot}$  and the mass of the companion  $(14.3 \pm 0.8) M_{\odot}$  (Mason et al. 2012). An updated ephemeris done by Falanga et al. (2015) resulted in a NS mass of  $(1.74 \pm 0.30) M_{\odot}$ , a mass of the companion of  $(17.5 \pm 0.8) M_{\odot}$  with a radius of  $(25 \pm 2) R_{\odot}$ . The NS is on a 10.447 29 d orbit around the companion star with an eclipse lasting 1.7 d. The eccentricity of the orbit is  $0.1075 \pm 0.0012$  (Jenke et al. 2012).

A possible cyclotron resonance scattering feature (see Section 5.2.4) of OAO 1657-415 was detected at approximately 36 keV, which would result in a magnetic field strength of  $3.1 \times 10^{12}$  G (Orlandini et al. 1999). This cyclotron line, however, could not yet be confirmed (see e.g. Pradhan et al. 2014). Other calculations of the magnetic field of the NS are based on different pulsar models (see e.g. Section 3). Jenke et al. (2012) gives a range of  $10^{12}$  G to  $10^{13}$  G for OAO 1657-415, while Yi et al. (1997a,b) calculates a magnetic field of about  $10^{13}$  G for a smooth transition between spin-up and spin-down and  $5 \times 10^{12}$  G for a sudden transition. By combining their model with observed quantities, Yi & Wheeler (1998) later find a magnetic field strength of  $2 \times 10^{13}$  G.

A long-term frequency history can be seen in Figure 2.5. As can be seen, OAO 1657-415 has been on a long-term spin-up trend with small-term torque reversals between MJD 43755 - 53946 (September 4, 1978 - July 30, 2006), resembling a sinusoid (Barnstedt et al. 2008).

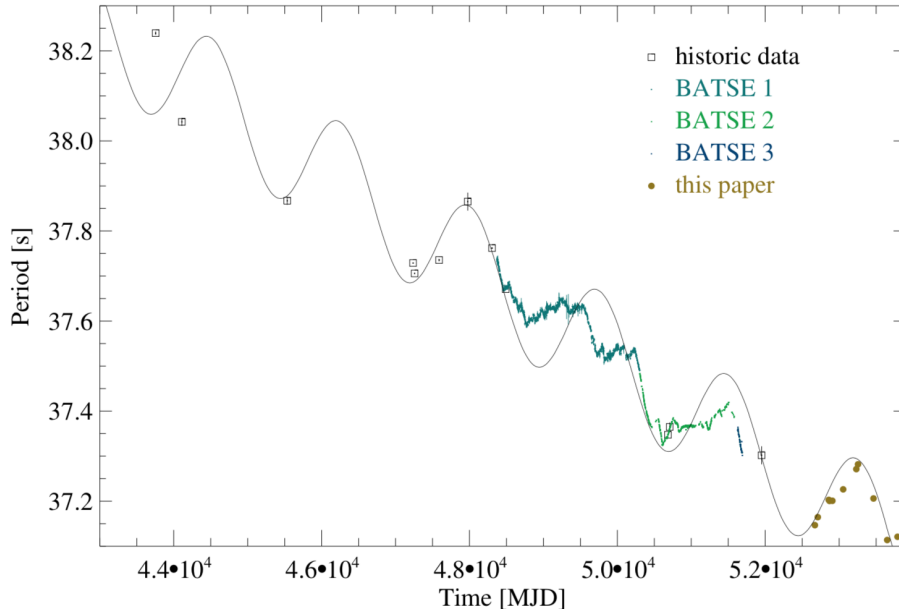


Figure 2.5: Pulse period history of OAO 1657-415. The sinusoidal function with a period of 4.8 yr is superposed on a linear long-term spin-up (Barnstedt et al. 2008).

## GX 1+4

GX 1+4 is in the constellation Ophiuchus (Oph) and it was discovered by Lewin et al. (1971) with an X-ray balloon experiment carried out in Australia in 1970. Its pulsations were periodically detected approximately every 2.3 min. GX 1+4 is part of a LMXB system with an M5 III giant donor star and the orbital period is believed to be of order years. From 1970 to 1980 the source was bright and spinning up, increasing in frequency from about 7.5 mHz to 9 mHz as can be seen in Figure 2.6a. In the early 1980s, it was decreasing in flux by two orders of magnitude and then rapidly spun down (Bildsten et al. 1997). This trend has continued since, see Figure 2.6b.

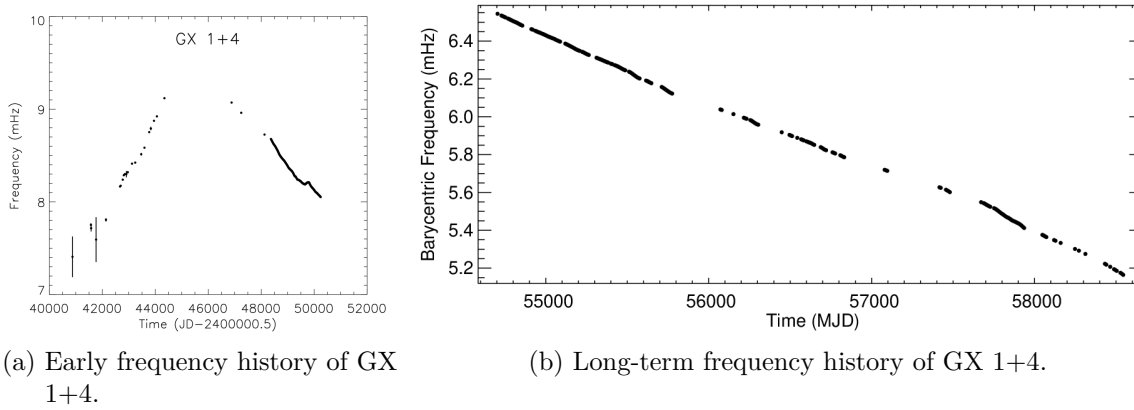


Figure 2.6: Frequency history of GX 1+4 (a) from Bildsten et al. (1997) and (b) from the *Fermi*/GMB Website (<https://gammaray.msfc.nasa.gov/gbm/science/pulsars.html>).

## 4U 1626-67

4U 1626-67 lies in the constellation Triangulum Australe (TrA) and it was discovered by the Uhuru satellite in 1972 (Giacconi et al. 1972; Chakrabarty et al. 1997b). It is listed in the fourth Uhuru catalog of X-ray sources (4U) (Forman et al. 1978). In 1977, 7.68 s pulsations were detected with the Small Astronomy Satellite 3 (SAS-3) (Rappaport et al. 1977). The optical companion was identified to be KZ TrA with a mass of  $< 0.1 M_{\odot}$ , as suggested by the orbital period of 42 min. Therefore 4U 1626-67 is a LMXB. As can be seen in Figure 2.7a, the NS has been steadily spinning up, corresponding to an increase in frequency until about 1991, when a spin-reversal commenced. From then onward, the NS was spinning down with approximately the same rate as it had spun-up before. The torque reversal was, however, not accompanied by a change in bolometric flux (Bildsten et al. 1997). After another torque reversal, the pulsar was again spinning up, a trend that still continues, as can be seen in Figure 2.7b.



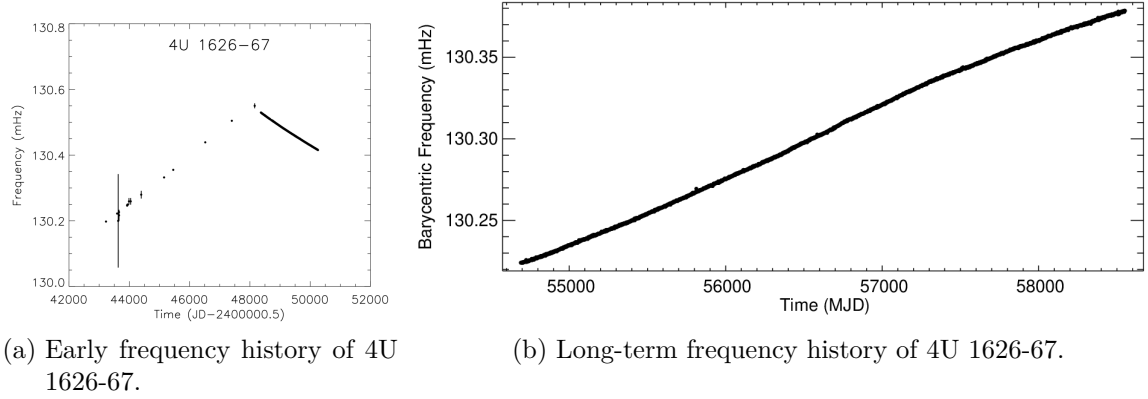


Figure 2.7: Frequency history of 4U 1626-67 (a) from Bildsten et al. (1997) and (b) from the *Fermi*/GMB Website (<https://gammaray.msfc.nasa.gov/gbm/science/pulsars.html>).



# Accretion-Torque Models

---

In an effort to explain the observed properties, such as the period changes described in Section 2.2, different models for accretion onto NSs have been proposed and over time expanded. In Section 3.1 the basic picture of accretion on magnetized objects is introduced and some characteristic radii are defined, Section 3.2 reviews the magnetic coupling between the star and the disk and its associated torques and in Section 3.3 an inclined rotator model, where the rotation and magnetic axes are misaligned, is presented.

## 3.1 Accretion on Magnetized Objects

The simplest model of accretion on magnetized objects will be described in the following.<sup>1</sup> Pulsars in XRBs can have strong magnetic fields, up to  $10^{15}$  G, which strongly influence the accretion flow. The magnetic field ( $B$ ) of a NS is dominantly of dipolar form

$$B \approx \frac{\mu}{r^3}, \quad (3.1)$$

where  $\mu$  [G cm<sup>3</sup>] denotes the magnetic dipole moment and  $r$  [cm] is the distance from the NS. In the simplest case of spherical accretion two opposing forces are present in the system: the magnetic pressure  $p_{\text{mag}}$ , caused by the magnetic field, and the ram pressure  $p_{\text{ram}}$ , which is the pressure of the infalling gas acting on the magnetic field. At the so-called Alfvén or magnetospheric radius,  $r_{\text{M}}$ , the magnetic and ram pressures are balanced, thus

$$\frac{1}{2}\rho v_{\text{ff}}^2 = \frac{B^2}{8\pi}, \quad (3.2)$$

where  $\rho$  is the density and the free-fall velocity is  $v_{\text{ff}} = (2GM/r)^{1/2}$ , with the gravitational constant  $G \approx 6.674 \times 10^{-8}$  cm<sup>3</sup> g<sup>-1</sup> s<sup>-2</sup>. In the case of spherical accretion, the mass accretion rate is given by  $\dot{M} = 4\pi r^2 \rho v_{\text{ff}}$  and  $r_{\text{M}}$  can be expressed as

$$r_{\text{M}} = \left( \frac{\mu^4}{2GM\dot{M}^2} \right)^{1/7} = 3.2 \times 10^8 \mu_{30}^{4/7} M_1^{-1/7} \dot{M}_{17}^{-2/7} \text{ cm}, \quad (3.3)$$

where  $\mu_{30}$  is the magnetic moment in units of  $10^{30}$  G cm<sup>3</sup>,  $M_1$  is the mass of the NS in units of  $1 M_{\odot}$  and  $\dot{M}_{17}$  is the mass accretion rate in units of  $10^{17}$  g s<sup>-1</sup>.

The dependence of  $r_{\text{M}}$  [cm] on the mass accretion rate  $\dot{M}$  [g s<sup>-1</sup>] is of particular importance. The larger the mass accretion rate is, the more pressure will be exerted by the material on the magnetic field and thus the smaller is the magnetospheric radius. The accreted matter approaches the NS in free-fall and on impact, its kinetic

---

<sup>1</sup>See e.g. Longair (2011); Shapiro & Teukolsky (1983); Bildsten et al. (1997); Vietri (2008); Perna et al. (2006); Revnivtsev & Mereghetti (2015).

energy is converted to radiation mostly in X-rays. Assuming a mass accretion rate  $\dot{M}$  [ $\text{g s}^{-1}$ ], and a NS with mass  $M \approx 1.4 M_\odot$  and radius  $R \approx 1.2 \times 10^6 \text{ cm}$ , the luminosity  $L_X$  is given by

$$L_X \approx \frac{GM\dot{M}}{R} \approx 1.5 \times 10^{20} \times \dot{M} \text{ erg s}^{-1}. \quad (3.4)$$

Furthermore, in the case of a spherical emitter, the luminosity can be expressed in terms of the distance  $d$  [cm] and the flux  $F$  [ $\text{erg s}^{-1} \text{ cm}^{-2}$ ]

$$L_X \approx 4\pi d^2 F \text{ erg s}^{-1}. \quad (3.5)$$

Thus, in the case of accretion from a disk, the magnetospheric radius can be expressed in terms of the flux observed.

The immediate vicinity of the NS is dominated by the magnetic field and this will dominate the accretion flow. The corotation radius is another essential radius in the system,

$$r_{\text{co}} = \left( \frac{GM}{\Omega_0^2} \right)^{1/3}, \quad (3.6)$$

which is the radius where the NS spin frequency  $\Omega_0$  is equal to the Keplerian frequency of the orbiting matter. Accretion can occur, when the magnetospheric radius is smaller than the corotation radius. If instead  $r_M > r_{\text{co}}$ , accretion will be reduced or stopped by the centrifugal barrier and matter might even be expelled in the so-called “propeller phase”. If the mass accretion rate from the companion changes over time, for example decreases, the magnetospheric radius will increase and eventually reach the corotation radius, inhibiting further accretion. This should be accompanied by a sudden drop in luminosity or transition into an unsteady accretion with large luminosity variations (Revnivtsev & Mereghetti 2015, and references therein).

It should be noted that a more accurate determination of the magnetospheric radius must take into account the exchange of angular momentum between the accretion disk and the NS. Vietri (2008) describes that at large distances from the NS, where the magnetic pressure is weak, the disk will drag the lines of the magnetic field along, thus creating a toroidal magnetic field in the disk.<sup>2</sup> This will create a torque acting on the disk material and thus a torque of the opposite sign will act on the NS. Another torque acting in the disk is the viscous torque. The magnetospheric radius is then the radius, where these torques are of the same magnitude. Vietri (2008) continues to define the poloidal field in the disk plane including a rough factor  $\eta \approx \text{const.}$ , thus getting

$$B_z = -\eta \frac{\mu}{r^3}. \quad (3.7)$$

By computing the magnetic and viscous torques, the condition for the magnetospheric radius can be found as

$$B_z(r_M) B_\phi(r_M) r_M^3 = -\frac{1}{2} \dot{M} \sqrt{GM r_M} \quad (3.8)$$

with the toroidal component  $B_\phi^3$  of the magnetic field

$$\frac{B_\phi}{B_z} = \frac{\gamma}{\alpha} \frac{\Omega_0 - \Omega_K}{\Omega_K} \quad (3.9)$$

<sup>2</sup>This toroidal field will have opposite sign inside as compared to outside the corotation radius (Equation (3.6)). For a more detailed discussion, see Vietri (2008).

<sup>3</sup>The toroidal component will be discussed in more detail in Section 3.2.2.

where  $\gamma \approx 1$  is a term that takes into account the details of the radial structure;  $\alpha$  is a numerical factor less than 1,  $\Omega_0$  is the angular velocity of the NS and  $\Omega_K$  is the angular velocity of the disk. With this, the magnetospheric radius is

$$r_M = 1.7 \times 10^8 \gamma^{2/7} \alpha^{-2/7} \dot{M}^{-2/7} M^{6/7} \eta^{-1} \mu_{30}^{4/7} \text{ cm.} \quad (3.10)$$

This equation is almost identical to Equation (3.3), except for a factor of order of magnitude one. Therefore Equation (3.3) is still a good approximation and will be used for the magnetospheric radius in the following.

## 3.2 Magnetic Coupling between the Star and Disk

### 3.2.1 The Basic Model by Ghosh & Lamb

Ghosh & Lamb (1978, 1979a,b, hereafter GL) developed a model for disk accretion including the magnetic coupling between the star and the disk. The GL model assumes an axis-symmetric disk accretion by an aligned rotator (see also Shapiro & Teukolsky 1983; Ögelman & van den Heuvel 1989). GL determine a broad transition zone that is caused by the field penetrating the disk. This transition zone connects the unperturbed disk to the magnetospheric flow near the star, see Figure 3.1.

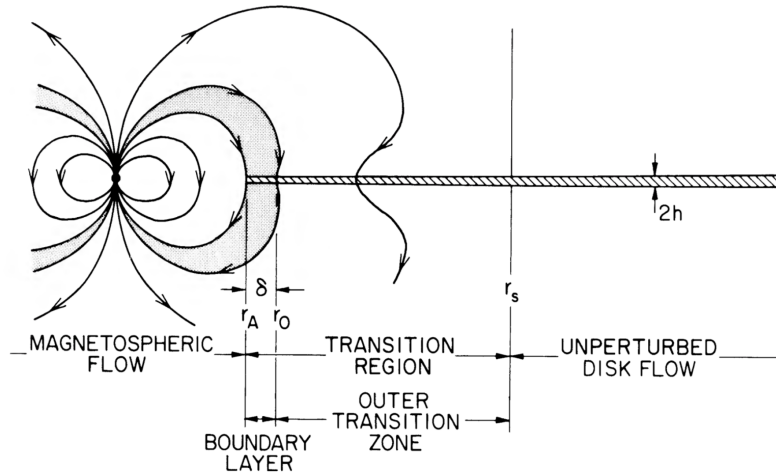


Figure 3.1: Illustration of the transition zone in the GL model, which connects the magnetospheric flow to the unperturbed disk. The magnetospheric radius is here denoted by  $r_A$  (Ghosh & Lamb 1978).

The radius  $r_0$ , where the velocity transitions from non-Keplerian to Keplerian was determined by GL to be

$$r_0 \approx 0.5 r_M. \quad (3.11)$$

GL find a simple relation between the spin-up of an accreting NS,  $-\dot{P}$  [s yr<sup>-1</sup>], and the product  $PL^{3/7}$ , where  $P$  [s] is the NS spin period and  $L$  [ergs s<sup>-1</sup>] its luminosity. The spin-up rate is an observed property which is a measure for the accreted angular momentum which depends on how matter is behaving outside the magnetosphere. Ghosh & Lamb (1979b) find the following expression for accretion from a disk

$$-\dot{P} = 5 \times 10^{-5} \mu_{30}^{2/7} n(\omega_s) S_1(M) (PL_{37}^{3/7})^2 \text{ s yr}^{-1}, \quad (3.12)$$

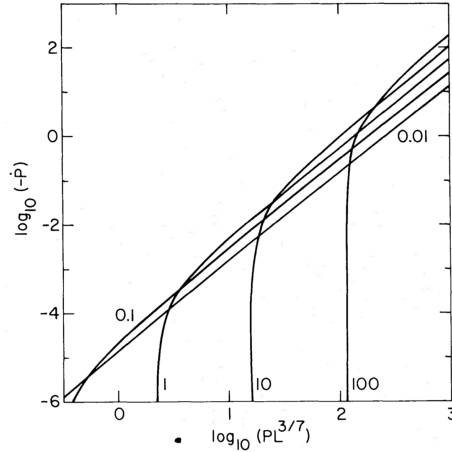


Figure 3.2: The spin-up rate  $-\dot{P}$  [s/yr] over the quantity  $PL^{3/7}$ , with the period  $P$  [s] and luminosity  $L$  [ $10^{37}$  erg s $^{-1}$ ]. The curves show different values of the magnetic moment in units  $10^{30}$  G cm $^3$  (Ghosh & Lamb 1979b).

where  $n(\omega_s)$  is a dimensionless torque,  $\omega_s$  is the fastness parameter (which is the ratio between the star's angular velocity and the angular velocity of the Keplerian disk at  $r_0$ ) and  $S_1(M)$  are defined as follows

$$\begin{aligned} n(\omega_s) &\approx 1.39\{1 - \omega_s[4.03(1 - \omega_s)^{0.173} - 0.878]\}(1 - \omega_s)^{-1}, \\ \omega_s &= 1.35 \mu_{30}^{6/7} S_2(M) (PL_{37}^{3/7})^{-1}, \\ S_1(M) &= R_6^{6/7} (M/M_\odot)^{-3/7} I_{45}^{-1}, \\ S_2(M) &= R_6^{-3/7} (M/M_\odot)^{-2/7}. \end{aligned}$$

The fastness parameter  $\omega_s$  determines whether a NS is a “fast rotator” ( $\omega_s \approx \omega_c$ ) or a “slow rotator” ( $\omega_s \ll 1$ ). Here,  $\omega_c$  is the critical fastness, below which the NS is spun-down by accretion.<sup>4</sup> In the slow rotator case, the magnetic coupling magnifies the spin-up torque experienced by the NS. For fast rotators on the other hand, the magnetic torque on the outer parts of the disk can oppose the spin-up torque and thus decrease the spin-up rate. Consequently, in the case of fast rotators (or in systems with low accretion rates), the NS might spin-down while matter is still accreted and thus beamed X-ray emission continues.

For slow rotators, thus large values of  $PL^{3/7}$ ,  $n(\omega_s)$  is constant and the system has a small dependence on  $\mu$ . In this region  $-\dot{P}$  goes as  $(PL^{3/7})^2$ , as can be seen in the log-log plot in Figure 3.2, where in this regime the relation is represented by a straight line with slope 2. With decreasing  $PL^{3/7}$ , the fastness parameter increases,  $n(\omega_s)$  decreases and the solution drops. At the critical fastness  $\omega_c$ ,  $\dot{P}$  is zero and thus its logarithm diverges. The point at which this happens depends on the magnetic moment as  $\mu^{6/7}$  (Ghosh & Lamb 1979b).

GL find a similar equation as Equation (3.12) for the case of wind accretion, that is

$$-\dot{P} = 3.8 \times 10^{-5} R_6 (M/M_\odot)^{-1} I_{45}^{-1} (l_a/10^{17} \text{ cm}^2 \text{ s}^{-1}) P^2 L_{37} \text{ s yr}^{-1}, \quad (3.13)$$

which, however, does not depend on the magnetic moment of the NS (Ghosh & Lamb 1979b).

<sup>4</sup>GL found  $\omega_c$  to be about 0.35, later work shows that it is more likely to be around 0.875 – 0.95 (Wang 1995).

### 3.2.2 An Improved Accretion-Disk Torque

Wang (1987) builds on the discussed GL model and also investigates the torque that is exerted on a NS assuming axis-symmetric disk accretion.<sup>5</sup> By comparing the time-scales of amplification and reconnection, GL estimated the strength of the toroidal magnetic field to be

$$\frac{B_\phi}{B_z} \approx \mp \frac{\gamma(\Omega_0 - \Omega_K)h}{\xi v_{Az}}, \quad (3.14)$$

where the upper sign is for  $z > 0$ ,  $\Omega_0$  and  $\Omega_K$  are the angular velocity of the NS and disk respectively,  $\gamma$  and  $\xi$  are numerical factors of order one and considerably less than unity respectively,  $h$  is the disk thickness and  $v_{Az}$  is the Alfvén velocity in the reconnecting field. Wang (1987) then discusses that in this case, the pressure caused by the wound field exceeds the thermal pressure beyond the corotation radius and would thus destroy the disk. Therefore, the azimuthal pitch of the field lines threading the disk needs to be smaller and was calculated to be

$$\frac{B_\phi}{B_z} \approx \mp \left| \frac{\gamma(\Omega_0 - \Omega_K)h}{\xi v_{Az}} \right|^{1/2}, \quad (3.15)$$

which is the square root of Equation (3.14). With this, the accretion-disk torque is then improved to include also large distances and the spin-up and spin-down contributions are calculated. The resulting torque calculated by Wang (1987) is then

$$-\frac{\dot{P}}{P} = 4.28 \times 10^{-5} f(x_0) \times P^{4/3} L_{37} M_{1.4}^{-4/3} R_6 \text{ yr}^{-1} \quad (3.16)$$

where

$$f(x_0) = x_0^{1/2} + \frac{2}{9} x_0^{31/80} \left[ 1 - x_0^{3/2} - \frac{x_0^{9/4}}{(1 - x_0^{3/2})^{1/2}} \right] \quad (3.17)$$

and  $x_0 = R_0/R_{\text{co}}$ . The magnetic dipole moment can then be calculated using

$$\mu_{30} = 6.16 \times 10^{-2} \frac{\alpha^{3/20}}{\eta} \left( \frac{\xi}{\gamma} \right)^{1/3} \frac{x_0^{211/120}}{(1 - x_0^{3/2})^{1/3}} P^{211/180} L_{37}^{8/15} \times M_{1.4}^{11/45} R_6^{8/15}, \quad (3.18)$$

where  $\eta$  is a screening factor assumed to be 0.2,  $\alpha$  is a measure for the ratio of the viscous shear stress and the thermal pressure, taken to be 0.3 and  $M_{1.4}$  is the mass of the NS in units  $1.4 M_\odot$ .

In a later paper, Wang (1995) studied the growth of the toroidal magnetic field considering additional effects. If the growth is limited by diffusive decay, caused by the turbulent mixing within the disk, the new azimuthal pitch is

$$\frac{B_\phi}{B_z} \approx \frac{\gamma(\Omega_0 - \Omega_K)}{\alpha \Omega_K}. \quad (3.19)$$

Under this assumption, the dimensionless torque  $n$ , that depends on the fastness parameter  $\omega_s$ , can be obtained

$$n(\omega_s) = \left( \frac{7}{6} - \frac{4}{3} \omega_s \right) / (1 - \omega_s). \quad (3.20)$$

---

<sup>5</sup>For a more in-depth description, see e.g. Bozzo et al. (2009, 2018).

Another effect that might limit the amplification of the toroidal magnetic field is the reconnection outside the disk, within the magnetosphere. Assuming the azimuthal pitch is limited to some maximum value  $\gamma_{\max}$ , this leads to

$$\frac{B_\phi}{B_z} = \begin{cases} \gamma_{\max}(\Omega_0 - \Omega_K)/\Omega_K, & \text{for } \Omega_K \geq \Omega_0; \\ \gamma_{\max}(\Omega_0 - \Omega_K)/\Omega_0, & \text{for } \Omega_K \leq \Omega_0. \end{cases} \quad (3.21)$$

The dimensionless torque is in this case

$$n(\omega_s) = \left( \frac{7}{6} - \frac{4}{3}\omega_s + \frac{1}{9}\omega_s^2 \right) / (1 - \omega_s), \quad (3.22)$$

where the equilibrium condition  $n(\omega_{\text{crit}}) = 0$  is true for  $\omega_{\text{crit}} = 0.950$  or  $R_0/R_c = 0.967$ . Wang (1995) discusses that the last case presented is the most plausible.

### 3.2.3 The Retrograde Disk Model

The accretion torque as a function of the mass accretion rate according to GL can be seen in Figure 3.3. Sudden transitions between spin-up and spin-down can only be possible if the mass accretion rate changes discontinuously. After GX 1+4 was observed to undergo such a transition, other interpretations were sought to explain these observations.

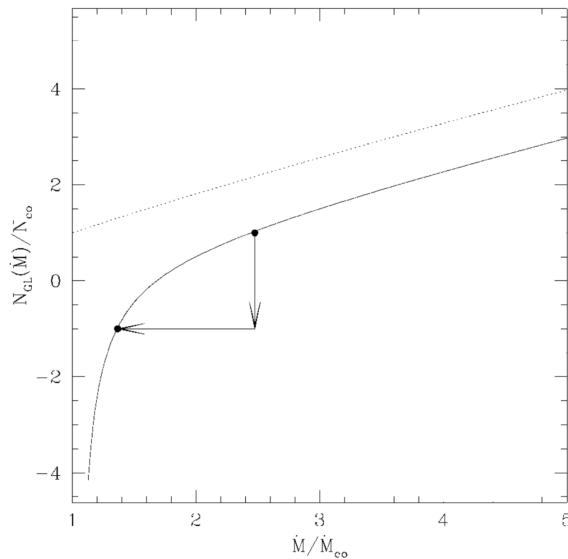


Figure 3.3: Sudden spin-up and spin-down transitions in the GL model require a step-like change of the mass accretion rate (Nelson et al. 1997).

Two-dimensional hydrodynamic calculations showed that a retrograde-rotating disc can form in wind-fed systems with a negative accreted angular momentum (Matsuda et al. 1987; Fryxell & Taam 1988). Makishima et al. (1988) suggested that this inversely rotating accretion disk might explain the observed transition in GX 1+4. A prograde accretion disk was first present during a spin-up period, which then dissipated before a new disk with reversed rotation formed, causing a spin-down. In systems with Roche lobe overflow, no mechanism has been suggested to explain how retrograde disks can appear (Nelson et al. 1997).



In the standard GL model, there is a correlation between torque and luminosity in the spin-up case (see Equation (3.12)), however no negative correlation is predicted in the spin-down region. Chakrabarty et al. (1997a), however, found a strong anti-correlation of the two quantities in GX 1+4, indicating that a retrograde accretion disk may be present and negative angular momentum might thus be transferred from the disk to the NS.

### 3.2.4 The Sub-Keplerian Disk Model

In the GL model, the torque can show a reversal when the mass accretion rate changes. A reversal can happen when the disk's inner edge passes the point of equilibrium, where the torque is zero. Only continuous (smooth) torque reversals can be explained with this model, unless there is a discontinuous (sudden) change of the mass accretion rate (see Section 3.2.3).

Sudden torque reversals have been observed in several pulsars, for example in GX 1+4 and 4U 1626-67, see Figures 2.6a and 2.7a respectively. These pulsars have shown a spin-up followed by a sudden torque reversal and subsequent spin-down phase in the past. In both pulsars, the the slope of the spin-up and spin-down phase is approximately the same but with opposite sign. Therefore, the magnitudes of the accretion torques  $|N_+|$  and  $|N_-|$  in the spin-up and spin-down phases respectively, are comparable,  $|N_+| \approx |N_-| \equiv |N|$ . To achieve this with the GL model, a fine-tuned step-like change in the mass accretion rate is required, see also Figure 3.3. The observed sudden reversals of the pulsars in 4U 1626-67, GX 1+4 and OAO 1657-415 with a nearly constant  $|N|$  can therefore not be well explained with this model.

Yi et al. (1997a) studied the spin evolution of these X-ray pulsars using a model including sub-Keplerian flow to explain the sudden (as opposed to smooth) torque reversals. In this model, a critical radius  $R_0$  exists outside of which the disk behaves Keplerian and within which the disk becomes sub-Keplerian, for a constant accretion rate. This transition has observational implications. The sub-Keplerian corotation radius will move inward and the inner disk edge will be relocated. This will cause the magnetic torque to change and a transition between spin-up and spin-down may be observed on a timescale less than a day, making it appear almost instantaneous (sudden).

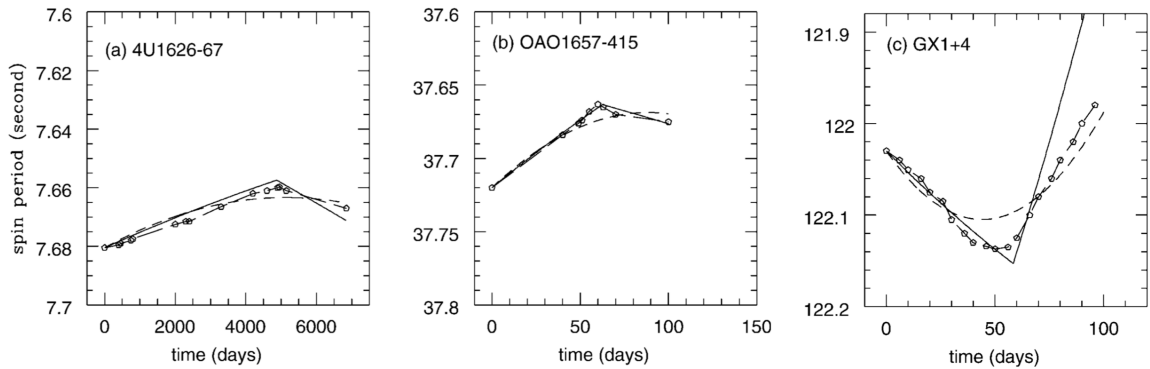


Figure 3.4: Observed torque reversals of three pulsars. The short-dashed lines show a smooth torque transition and the thick solid lines the sudden transitions as presented by Yi et al. (1997b).

The computation of a spin evolution can be seen in Figure 3.4, yielding results of the magnetic field ( $B$ ), mass accretion rate ( $\dot{M}$ ) and critical mass accretion rate ( $\dot{M}_{\text{crit}}$ ) for the studied pulsars as presented in Table 3.1. The critical mass accretion rate is the rate where the sudden transition is most likely to occur.

Table 3.1: Results for three pulsars from Yi et al. (1997a,b). The smooth and sudden transitions were calculated and the magnetic fields ( $B$ ) and mass accretion rates ( $\dot{M}$ ) were computed. The critical accretion rate ( $\dot{M}_{\text{crit}}$ ), where the sudden transition is most likely to occur, was also determined.

Object	Smooth transition		Sudden transition		
	$B$ [G]	$\dot{M}$ [ $\text{g s}^{-1}$ ]	$B$ [G]	$\dot{M}$ [ $\text{g s}^{-1}$ ]	$\dot{M}_{\text{crit}}$ [ $\text{g s}^{-1}$ ]
4U 1626-67	$10^{12}$	$4.2 \times 10^{16}$	$6 \times 10^{11}$	$2.8 \times 10^{16}$	$2.2 \times 10^{16}$
OA0 1657-415	$10^{13}$	$2 \times 10^{17}$	$5 \times 10^{12}$	$1.2 \times 10^{17}$	$1.0 \times 10^{17}$
GX 1+4	$4 \times 10^{13}$	$10^{15}$	$1.3 \times 10^{13}$	$4 \times 10^{16}$	$6 \times 10^{16}$

### 3.3 The Inclined Rotator Model

The following section is based on the paper by Perna et al. (2006, hereafter PBS). Assuming the  $z$ -axis of a cylindrical coordinate system with  $(r, \phi, z)$  coincides with the rotation axis of the NS, an inclination angle  $\chi$  can be defined between this rotation axis and the magnetic moment of the NS, as illustrated in Figure 3.6a. The magnetic field in the disk plane is, under the assumption that the disk is planar and its axis is parallel to the  $z$ -axis,

$$B^2 = \frac{\mu^2}{r^6} [1 + 3(\sin \chi \sin \phi)^2], \quad (3.23)$$

where  $\mu$  [ $\text{G cm}^3$ ] is the magnetic moment and  $r$  [cm] the distance from the NS.<sup>6</sup> Thus, if  $\chi \neq 0$  the magnetic field strength will depend on the phase angle  $\phi$ , resulting also in an asymmetric magnetospheric radius, as illustrated in Figure 3.5 and explained below.

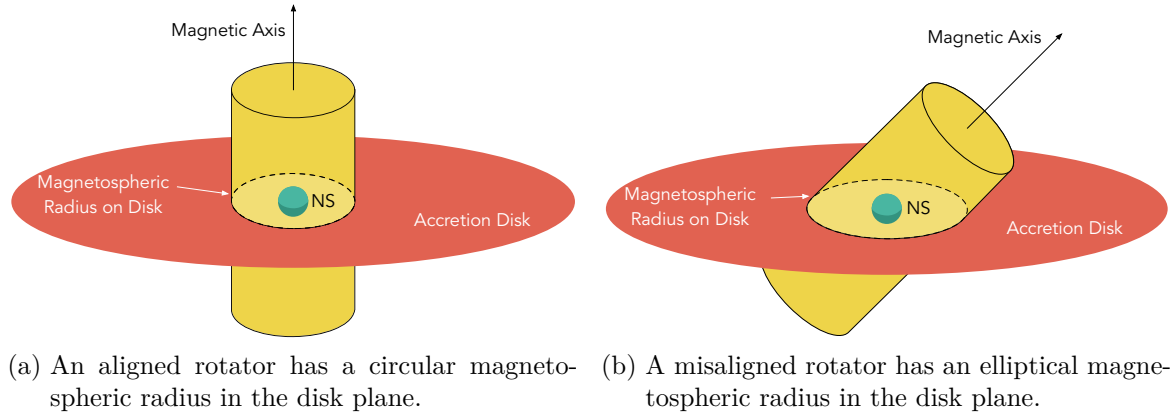


Figure 3.5: Schematic representation of an (a) aligned and (b) misaligned rotating NS and how it affects the shape of the projection of the magnetospheric radius in the disk plane. The yellow cylinder has no actual physical meaning and serves only to illustrate the effect of the inclination on the magnetospheric radius in the disk plane.

The magnetospheric radius of an oblique rotator in the disk plane is therefore adapted from equation (3.3) to take into account the inclination and phase angle

$$R_M(\phi) = 3.2 \times 10^8 \mu_{30}^{4/7} M_1^{-1/7} \dot{M}_{17}^{-2/7} [1 + 3(\sin \chi \sin \phi)^2]^{2/7} \text{cm}, \quad (3.24)$$

where  $M_1$  is the mass of the NS in units  $1 M_\odot$  and  $\dot{M}$  [ $\text{g s}^{-1}$ ] is the mass accretion rate. In Figure 3.6b a schematic representation of the magnetospheric radius in the disk plane can be seen in dependence on the phase angle  $\phi$ .

In an aligned rotator, the system can be either in the propeller, or in the accreting state (see Section 3.1), while in the oblique case, it can be in both states simultaneously at different phase angles  $\phi$ .

PBS introduces an ejection radius, beyond which matter can be unbound from the system through the propeller mechanism, which is larger than the corotation radius. Therefore there is a region between the corotation and ejection (or “infinity”) radius,  $R_{\text{inf}}$ , where matter is ejected from the system but does not have enough energy to

<sup>6</sup>See Equation (3.1) for the axisymmetric equivalent.

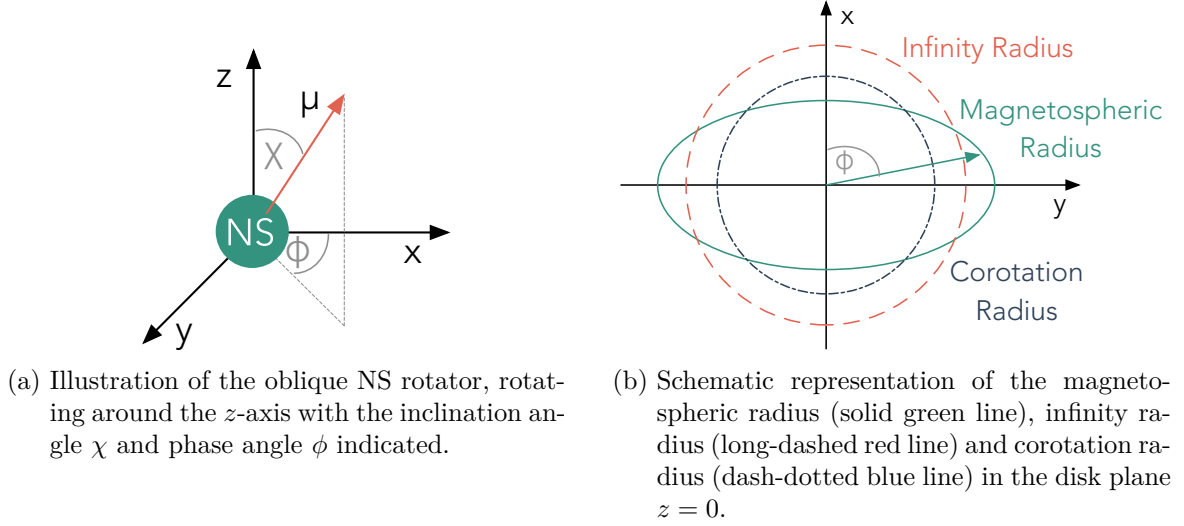


Figure 3.6: Schematic illustration of the oblique NS rotator, where the magnetic moment  $\mu$  is inclined with respect to the rotation-/ $z$ -axis (a) and the magnetospheric, infinity and corotation radii in the disk plane (b). Adapted from Perna et al. (2006).

completely unbind. Instead, this matter falls back onto the disk and then restarts its motion toward the NS. By introducing an elasticity parameter  $\beta$ , which indicates how efficiently kinetic energy of the NS is converted via the magnetosphere-disk interaction into kinetic energy of the ejected matter, a generalized rotational velocity can be defined

$$v_{\text{gen}} = \Omega_K(R_M)R_M(1 - \gamma), \quad (3.25)$$

where  $\Omega_K$  is the Keplerian velocity and  $\gamma$  is a dimensionless parameter defined as

$$\gamma = (1 + \beta) \left( 1 - \frac{\Omega_0}{\Omega_K} \right). \quad (3.26)$$

Here  $\beta = 1$  represents the limit of the totally elastic case while  $\beta = 0$  indicates the inelastic case. The infinity radius can then be derived as

$$R_{\text{inf}} = \left( \frac{\beta + \sqrt{2}}{1 + \beta} \right)^{2/3} R_{\text{co}}. \quad (3.27)$$

This infinity radius is also shown in Figure 3.6b. Therefore, three regimes can be present in the system at the same time, depending on the inclination angle  $\chi$  and phase  $\phi$ :

- Accretion can happen where  $R_M(\phi, \chi) < R_{\text{co}}$ ,
- matter is ejected to larger radii if  $R_{\text{co}} < R_M(\phi, \chi) < R_{\text{inf}}$ , and/or
- matter can be unbound from the system and thus be ejected to infinity, where  $R_M(\phi, \chi) > R_{\text{inf}}$ .

The inflowing matter from the donor star ( $\dot{M}_*$ ) is accreted through one of the accretion processes discussed in Section 2.1.1. For a given inclination angle  $\chi$ , the fraction

of matter that is accreted, recycled or ejected will be proportional to the angle  $\phi$ , as indicated in Figure 3.6b. The components are calculated using

$$\dot{M}_{\text{comp}} = \frac{1}{2\pi} \int_{\phi_1}^{\phi_2} d\phi \frac{d\dot{M}_{\text{tot}}}{d\phi}, \quad (3.28)$$

where “comp” stands for the different components of accreted (“acc”), recycled (“rec”) and ejected (“eje”) matter and the integration interval  $[\phi_1, \phi_2]$  spans over the corresponding above mentioned regions.

The total mass available to the system is the mass that is captured by the companion star,  $\dot{M}_*$ , which is, due to mass conservation,

$$\dot{M}_* = \dot{M}_{\text{acc}} + \dot{M}_{\text{eje}}. \quad (3.29)$$

The magnetospheric radius  $R_M$  is however determined by the total pressure of the accreting matter, which includes the additional term of the recycled matter

$$\dot{M}_{\text{tot}} = \dot{M}_{\text{acc}} + \dot{M}_{\text{eje}} + \dot{M}_{\text{rec}}. \quad (3.30)$$

The different components of the mass rates are schematically shown in Figure 3.7.

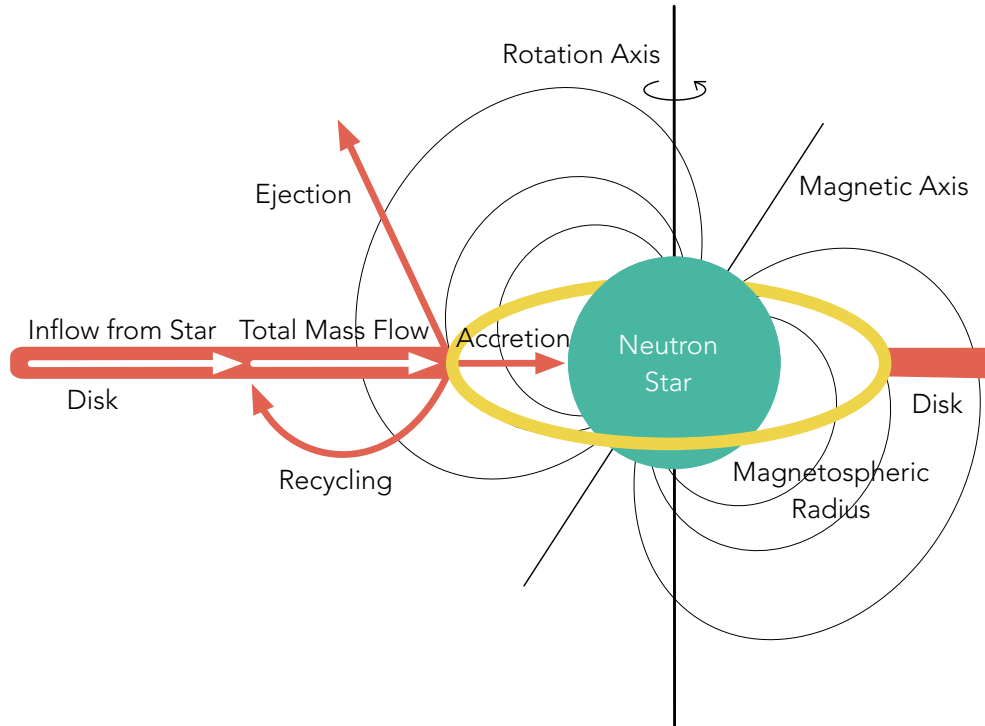


Figure 3.7: Schematic representation of the mass flow rate components in the inclined rotating NS system: mass inflow rate from the donor star ( $\dot{M}_*$ ), total mass flow rate ( $\dot{M}_{\text{tot}}$ ), mass accretion rate ( $\dot{M}_{\text{acc}}$ ), ejected mass flow rate ( $\dot{M}_{\text{eje}}$ ) and the recycled component ( $\dot{M}_{\text{rec}}$ ). Also shown is the magnetospheric radius ( $r_M$ ) in yellow, magnetic field lines, the rotation and magnetic axes in black, as well as the accretion disk in red. Adapted from Perna et al. (2006).

Including the recycled component of the matter can thus lead to smaller values of  $\dot{M}_*$  for which matter can be accreted. This can be visualized by plotting  $\dot{M}_*$  over

the total mass rate  $\dot{M}_{\text{tot}}$ , see Figure 3.8. The mass of the NS was assumed to be  $M = 1.4 M_{\odot}$  and the radius  $R = 10 \text{ km}$ , all other fixed parameters are shown in the Figure. The quantity that is varied is the mass inflow from the companion,  $\dot{M}_*$ . The Figure shows that one or more solutions can be adopted for a constant  $\dot{M}_*$  and which state the system is in will depend on its previous history. Thus a hysteresis-type loop can exist and the solution might jump discontinuously from one place to another for a continuous variation of  $\dot{M}_*$ .

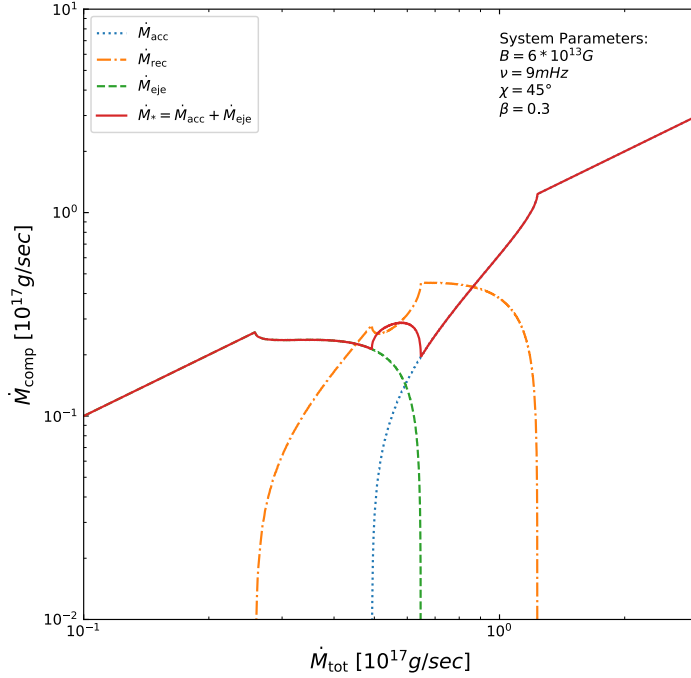


Figure 3.8: Contributions to the total mass flow rate  $\dot{M}_{\text{tot}}$ . For low values of  $\dot{M}_{\text{tot}}$ , all matter will be ejected and for large values of  $\dot{M}_{\text{tot}}$  all matter will be accreted. In-between, some of the matter will be recycled, changing  $r_M$  and causing a hysteresis-type loop. Adapted from Perna et al. (2006).

Only the accreted and ejected material will contribute to the net angular momentum transferred between the disk and the NS. The change of angular momentum of the NS can thus be calculated as

$$\frac{d\Omega_0}{dt} = \frac{\dot{M}_{\text{tot}}}{2\pi} \frac{1}{I} \int_0^{2\pi} (GM R_M)^{1/2} \left\{ 1 - \theta(R_M - R_{\text{co}}) \left[ 1 + (1 + \beta) \left( \frac{\Omega_0}{\Omega_K} - 1 \right) \right] \right\} d\phi, \quad (3.31)$$

where  $I$  is the NS moment of inertia,  $G$  is the gravitational constant,  $M$  is the mass of the NS and  $\theta(R_M - R_{\text{co}})$  is 1 for  $R_M > R_{\text{co}}$  and 0 otherwise. Equation (3.31) can be expressed as a change in frequency via  $d\Omega_0/dt = 2\pi\dot{\nu}$ .

The total luminosity of the system can be calculated from its separate contributions. The accreted component is given by the energy released from the matter falling from the magnetospheric radius to the surface of the NS, thus

$$L_{\text{acc}} = \int_{R_M < R_{\text{co}}} \left[ GM \left( \frac{1}{R_{\text{NS}}} - \frac{1}{R_M} \right) + \frac{1}{2} \Omega_0^2 (R_M^2 - R_{\text{NS}}^2) \right] d\dot{M}_{\text{acc}}. \quad (3.32)$$

The luminosity contribution from the recycled matter can be calculated from the

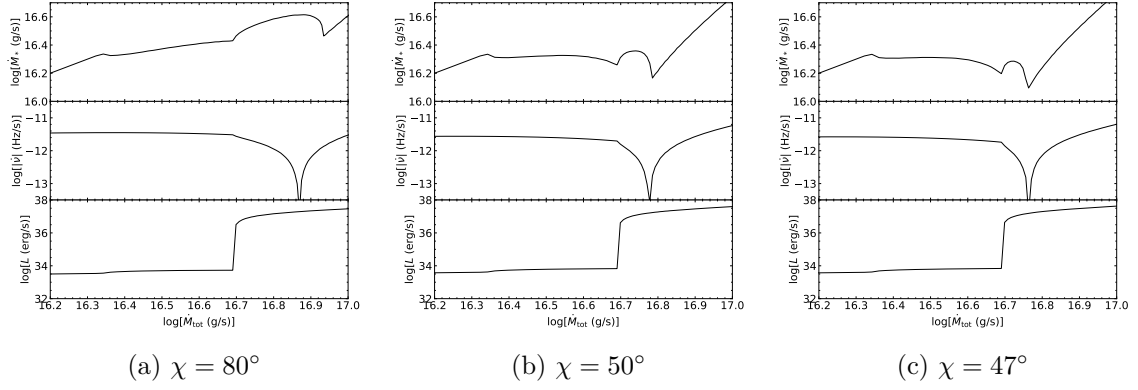


Figure 3.9: Different hysteresis limit cycles as they can also be found in Perna et al. (2006). In all cases the system parameters are  $\nu = 9 \text{ mHz}$ ,  $B = 6 \times 10^{13} \text{ G}$  and  $\beta = 0$ . The inclination angle  $\chi$  is varied.

luminosity of the energy released at  $R_K$ , where it falls back on the disk, and that of the matter moving back inwards to  $R_M$ ,

$$L_{\text{rec}} = \int_{R_{\text{co}} < R_M < R_{\text{inf}}} \left( \frac{v_{\text{gen}}^2}{2} - \frac{GM}{2R_M} \right) d\dot{M}_{\text{rec}}. \quad (3.33)$$

There also exists a luminosity component at the boundary layer separating the magnetosphere and the disk, which is for an arbitrary elasticity parameter

$$L_{\text{BL}} = \begin{cases} \frac{\dot{M}_{\text{tot}}}{4\pi} \int_0^{2\pi} [R_M^2 (\Omega_K^2 - \Omega_0^2)] d\phi & \text{for } R_M < R_{\text{co}}, \\ \frac{\dot{M}_{\text{tot}}}{4\pi} (1 - \beta) \int_0^{2\pi} [R_M^2 (\Omega_0^2 - \Omega_K^2)] d\phi & \text{for } R_M \geq R_{\text{co}}. \end{cases} \quad (3.34)$$

Lastly, there is a component from the disk in all regions

$$L_{\text{disk}} = \frac{GM\dot{M}_*}{2R_M}. \quad (3.35)$$

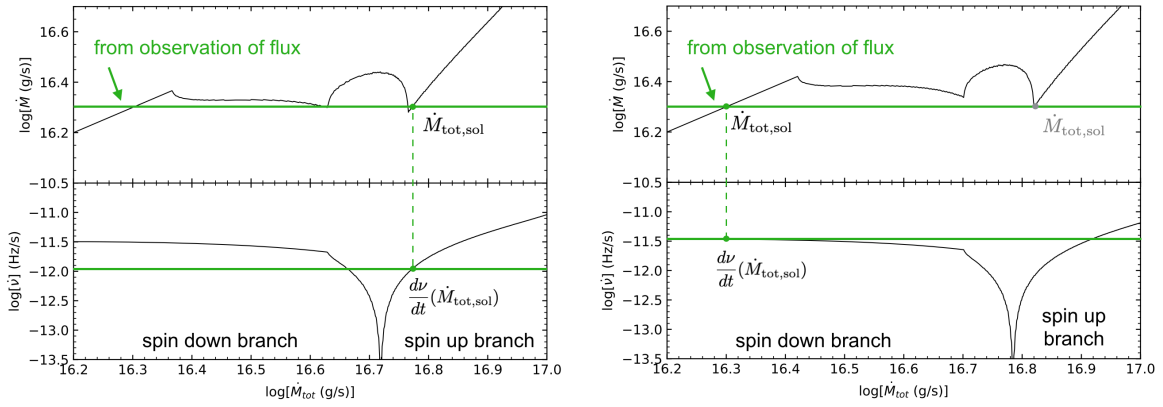
Both equation (3.31) and the superposition of equations (3.32) - (3.35) were plotted alongside the  $\dot{M}_*$  over  $\dot{M}_{\text{tot}}$  plot and the results for different values of the inclination angle  $\chi$  can be seen in Figure 3.9. In fact, the existence of a hysteresis limit cycle depends on the angle  $\chi$ , which has to be large enough for both the accretion and propeller regime to be present in the system. The shape of the  $\dot{M}_*$  curve changes with the inclination angle  $\chi$ . The torque can be seen in the middle panels of Figure 3.9 where the left side of the drop corresponds to a spin-down branch and the right side to a spin-up branch. The bottom panel shows the luminosity. Figure 3.9a shows that a reversal from spin-up to spin-down and vice versa is accompanied by a luminosity change within an order of magnitude. Figure 3.9b depicts a reversal coupled to a luminosity variation of over three orders of magnitude and in 3.9c the luminosity is considerably larger on the spin-up branch than on the spin-down branch.

PBS now assumes that the accretion mechanism happens through Roche lobe overflow which leads to a roughly constant mass supply rate ( $\dot{M}_*$ ). The system can then reach a cyclic spin-up/spin-down state as follows (see Figure 3.10). Suppose the NS

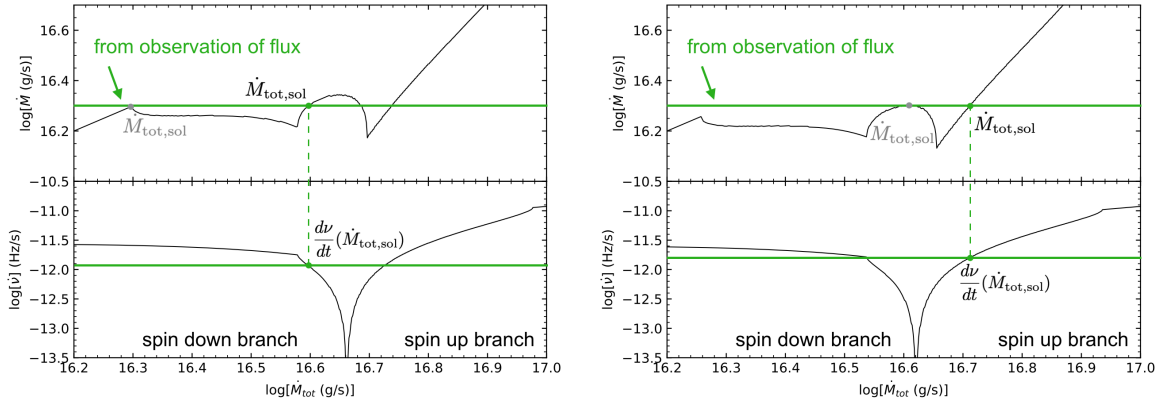
spins with a certain frequency ( $\nu$ ), is spinning-up and a flux is measured, which can then be converted to a mass inflow rate via Equations (3.4) and (3.5). The solution for these initial conditions can be found on the  $\dot{M}_* - \dot{M}_{\text{tot}}$  plot and the corresponding value for  $\dot{\nu}$  may be found. With this value, a new frequency at the next computed time step can be determined as

$$\nu(t + dt) = \nu(t) + \frac{d\nu(\dot{M}_{\text{tot},\text{sol}})}{dt}, \quad (3.36)$$

where  $\dot{M}_{\text{tot},\text{sol}}$  refers to the “solution” state, see also Figure 3.10. The higher frequency then leads to a translation of the  $\dot{M}_* - \dot{M}_{\text{tot}}$  curve toward the upper right and the new solution will be found until there is no solution to be found on the spin-up branch and the system transitions to the spin-down branch.



- (a) The initial conditions of the system are an observed frequency  $\nu$  on the spin-up branch with a constant mass inflow rate  $\dot{M}_*$  as estimated from the observed flux. (b) The system is spinning-up until there is no more solution on the spin-up branch.



- (c) The system is on the spin down branch. (d) Another torque reversal, now from spin-down to spin-up.

Figure 3.10: Time evolution of a system with a constant mass inflow rate  $\dot{M}_*$ . The previous states of the system are indicated in gray in (b)-(d).



With this method, PBS studied the X-ray pulsars GX 1+4 and 4U 1626-67 (see Section 2.2.2). The results can be seen in Figure 3.11<sup>7</sup> and the determined parameters are summarized in Table 3.2.

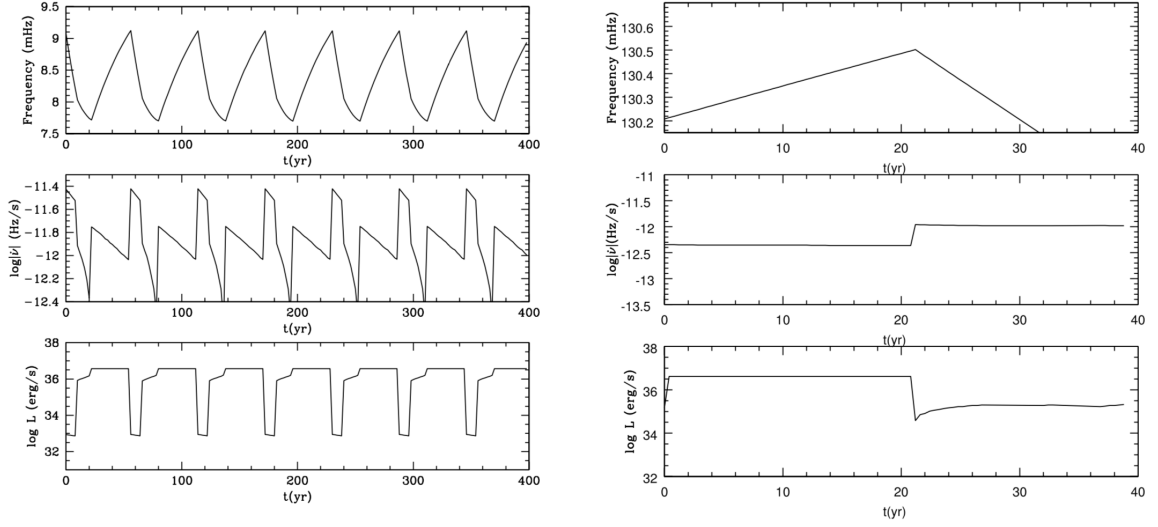


Figure 3.11: Results found for GX 1+4 (left) and 4U 1626-67 (right) (Perna et al. 2006). The determined parameters can be seen in Table 3.2.

Table 3.2: Parameters as determined by the PBS model for GX 1+4 and 4U 1626-67.

	GX 1+4	4U 1626-67
Magnetic field $B$	$6 \times 10^{13} \text{ G}$	$2.5 \times 10^{12} \text{ G}$
Inclination angle $\chi$	$45^\circ$	$68^\circ$
Elasticity parameter $\beta$	0.3	0.0

<sup>7</sup>Compare this to the observations that can be seen in Figures 2.6a and 2.7a.



# Applying an Inclined Accretion Torque Model to OAO 1657-415

---

The accretion torque model developed by Perna et al. (2006, hereafter PBS) and presented in Section 3.3 explains sudden torque reversals in XRBs with similar magnitude of spin-up/spin-down and different variabilities in luminosity. The observed behavior of GX 1+4 and 4U 1626-67 were in its most distinct features explained by the model and parameters such as the magnetic field and inclination angle were roughly estimated. It is thus reasonable to apply the model to other sources with similar characteristics as well. In the following numerical calculations, the mass of the NS was assumed to be  $1.4 M_{\odot}$  and the radius 10 km.

## 4.1 Exploration of the Model

The parameters that can be adjusted in the PBS model are the magnetic field strength ( $B$ ), the inclination angle ( $\chi$ ), the initial frequency ( $\nu$ ), the elasticity parameter ( $\beta$ ) and the mass supply from the donor star ( $\dot{M}_*$ ). As can be easily understood from the time evolution plot in Figure 3.10, the mass supply from the donor star  $\dot{M}_*$ , which is directly proportional to the observed flux (see Equations (3.4) and (3.4)), determines the points of torque reversal and is thus coupled to the initial frequency ( $\nu$ ), which in turn is an observable property. To understand the influence of the other parameters, Figures 4.1 and 4.2 show several variations, as discussed in the following.

In Figure 4.1 the inclination angle  $\chi = 45^\circ$  and elasticity parameter  $\beta = 0.3$  are fixed. Furthermore, Figures (a)-(c) have a constant magnetic field of  $B = 6 \times 10^{13}$  G and (d)-(f) show  $B = 1 \times 10^{14}$  G. Both rows with constant magnetic field then show an increasing initial frequency from 6 mHz to 12 mHz. Let  $\nu_{\text{eq}}$  be the “equilibrium” (average) frequency between points of torque reversal,  $\Delta\nu_{\text{eq}}$  its amplitude and  $\Delta T_{\text{eq}}$  the timescale for one cycle. Figure 4.1 (b) shows torque reversals between 7.5 mHz to 9 mHz, thus  $\nu_{\text{eq}} = 8.25$  mHz,  $\Delta\nu_{\text{eq}} = 1.5$  mHz and  $\Delta T_{\text{eq}} = 64$  yr. It can then be seen that by choosing a frequency not close to  $\nu_{\text{eq}}$  and outside of the range of torque reversals, the system first needs to spin-up (a) or spin-down (c) to reach this equilibrium. The same principle holds for Figures (d)-(f) where the equilibrium frequency is  $\nu_{\text{eq}} = 5.35$  mHz,  $\Delta\nu_{\text{eq}} = 0.9$  mHz and  $\Delta T_{\text{eq}} = 37$  yr. A summary for both magnetic fields and the determined parameters can be seen in Table 4.1. It can be deduced that an increase of magnetic field lowers the equilibrium frequency, the amplitude and the timescale of torque reversals.

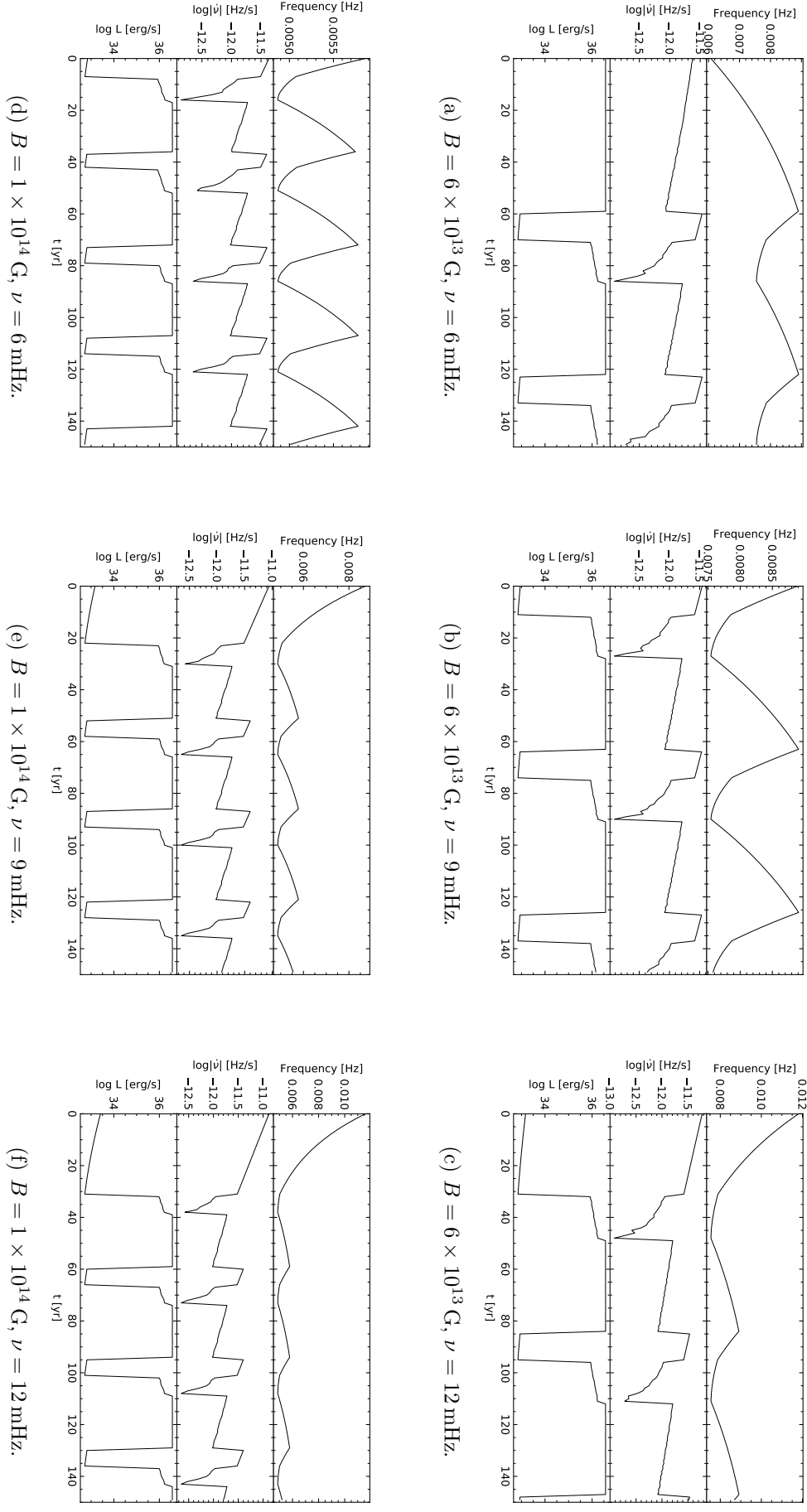


Figure 4.1: Comparison of the frequency, frequency derivative and luminosity histories of different parameters. The angle  $\chi = 45^\circ$  and elasticity parameter  $\beta = 0.3$  are the same for all panels, the initial frequency ( $\nu$ ) and magnetic field ( $B$ ) are modified as indicated.

Table 4.1: Equilibrium frequency ( $\nu_{\text{eq}}$ ), amplitude ( $\Delta\nu_{\text{eq}}$ ) and timescale of variability ( $\Delta T_{\text{eq}}$ ) for the two magnetic field strengths ( $B$ ) of Figure 4.1.

$B$ [G]	$\nu_{\text{eq}}$ [mHz]	$\Delta\nu_{\text{eq}}$ [mHz]	$\Delta T_{\text{eq}}$ [yr]
$6 \times 10^{13}$	8.25	1.5	64
$1 \times 10^{14}$	5.35	0.9	37

Figure 4.2 shows the results for a constant initial frequency  $\nu = 9$  mHz but varying

- magnetic field:  $B = 6 \times 10^{13}$  G in (a)-(c) and  $B = 1 \times 10^{14}$  G in (d)-(f),
- inclination angle:  $\chi = 45^\circ$  in (a), (b), (d), (f) and  $\chi = 60^\circ$  in (c), (e) and
- elasticity parameter:  $\beta = 0.8$  in (a), (d) and  $\beta = 0.3$  in (b), (c), (e), (f).

The determined parameters  $\nu_{\text{eq}}$ ,  $\Delta\nu_{\text{eq}}$ ,  $\Delta T_{\text{eq}}$  and additionally the order of magnitude variation of the luminosity  $\Delta L$  for these cases are shown in Table 4.2. According to these results

- for constant  $B$  and  $\chi$ , but decreasing  $\beta$ , the equilibrium frequency, its amplitude, timescale and luminosity variability increase;
- for constant  $B$  and  $\beta$ , with increasing angle  $\chi$ , the equilibrium frequency, its amplitude and luminosity variability decrease while the timescale between torque reversals increases.

Table 4.2: Estimates of the equilibrium frequency ( $\nu_{\text{eq}}$ ), amplitude ( $\Delta\nu_{\text{eq}}$ ), timescale of variability ( $\Delta T_{\text{eq}}$ ) and order of magnitude of the luminosity change ( $\Delta L$ ) for two magnetic field strengths ( $B$ ).

Fig.	$B$ [G]	$\chi$	$\beta$	$\nu_{\text{eq}}$ [mHz]	$\Delta\nu_{\text{eq}}$ [mHz]	$\Delta T_{\text{eq}}$ [yr]	$\Delta L$ [erg s $^{-1}$ ]
4.2 (a)	$6 \times 10^{13}$	$45^\circ$	0.8	6.90	0.8	57	1.0
4.2 (b)	$6 \times 10^{13}$	$45^\circ$	0.3	8.25	1.5	64	3.8
4.2 (c)	$6 \times 10^{13}$	$60^\circ$	0.3	6.80	0.4	66	0.7
4.2 (d)	$1 \times 10^{14}$	$45^\circ$	0.8	4.45	0.7	30	0.7
4.2 (e)	$1 \times 10^{14}$	$45^\circ$	0.3	5.35	0.9	37	3.8
4.2 (f)	$1 \times 10^{14}$	$60^\circ$	0.3	4.40	0.8	40	1.0

Thus, in order to get a specific combination of the timescale of torque reversal, luminosity variability, equilibrium frequency and corresponding frequency amplitude, the parameters  $\chi$ ,  $B$  and  $\beta$  need to be chosen carefully. Generally speaking, the increase of the magnetic field shortens the time of torque reversal while the parameters  $\chi$  and  $\beta$  change the equilibrium frequency and luminosity variability, where a larger  $\chi$  or smaller  $\beta$  lead to smaller luminosity changes. Since all parameters are interconnected however, it may not always be possible to find parameters corresponding to a fixed set of observed properties.

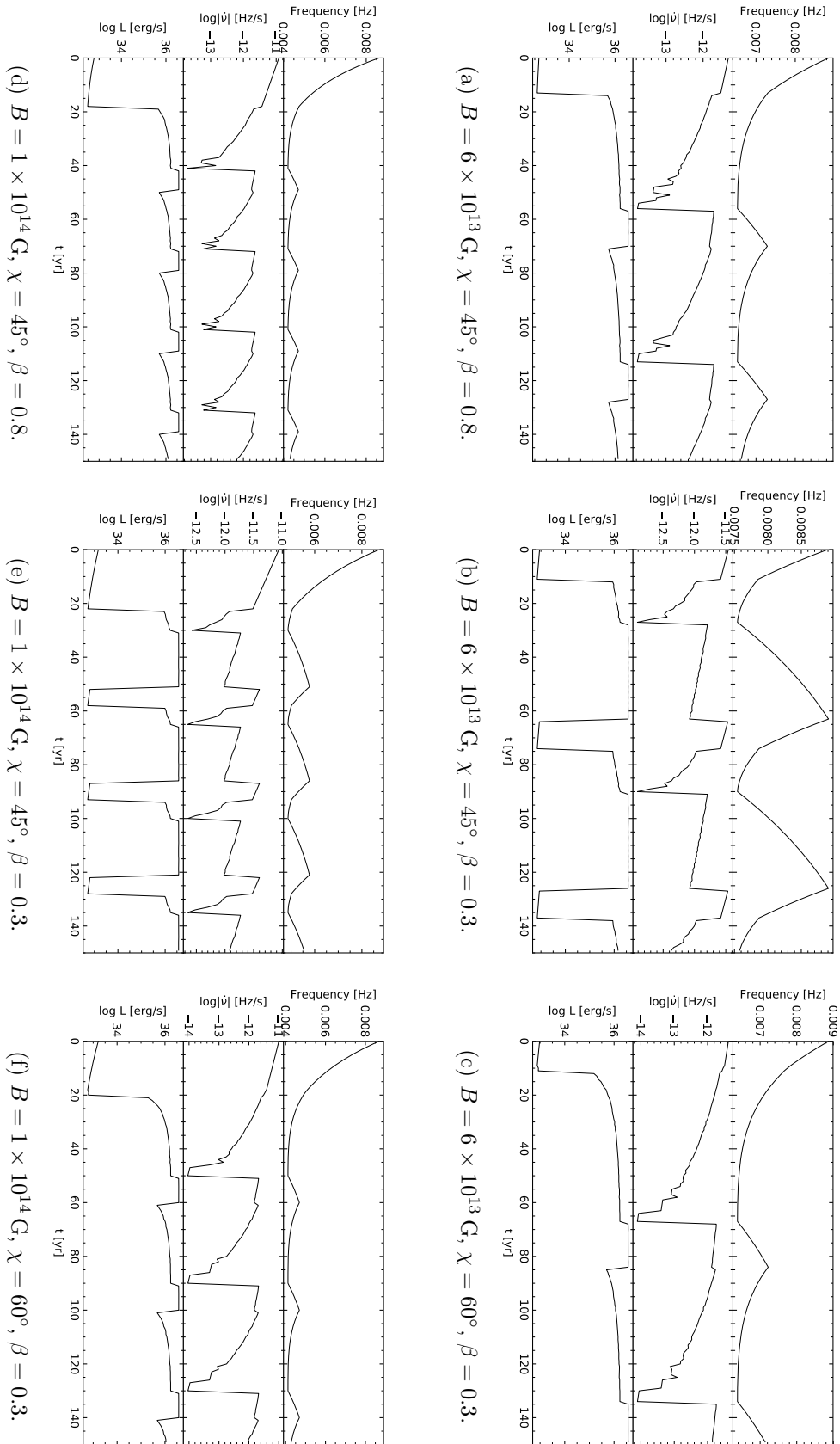


Figure 4.2: Comparison of the frequency, frequency derivative and luminosity histories of different parameters. The initial frequency  $\nu = 9 \text{ mHz}$  is the same for all panels, the inclination angle ( $\chi$ ), elasticity parameter ( $\beta$ ) and magnetic field ( $B$ ) are modified.

## 4.2 Introducing a Time Variable $\dot{M}_*$

As was mentioned before, the pulse period history of the pulsar in OAO 1657-415 was approximated by a sinusoid superposed on a linear spin-up trend, see Figure 2.5 (Barnstedt et al. 2008). The Perna et al. (2006) model did not include this superposition, but a time variable  $\dot{M}_*$  can create this type of behavior, as further explored below.

It is feasible that a change in  $\dot{M}_*$  could be caused by a changing mass loss rate of the companion. The mass loss rates of Wolf-Rayet stars (including WNL stars such as the one in OAO 1657-415) are, however, not known with great precision (Maeder & Meynet 1994). Yi & Wheeler (1998) discuss how else a variability of  $\dot{M}_*$  on timescales of a year to a few decades can occur. One idea is that an X-ray irradiation-induced, mass-flow oscillation can create long-term oscillations when certain conditions, e.g. the disk size and specific  $\alpha$  values for the disk, are met. Another suggestion is that a long-term variation can be caused by disk instabilities. It is therefore reasonable to assume that  $\dot{M}_*$  may not always be constant but could change with time.

A modulation of the mass loss rate  $\dot{M}_*$  of the companion is needed in the model by Yi et al. (1997a,b); Yi & Wheeler (1998), see also Section 3.2.4. To achieve the desired torque reversals, as seen in Figure 3.4, the following changes of the mass loss rate were required (Yi et al. 1997a,b):

- 4U 1626-67:  $d\dot{M}/dt = -4.5 \times 10^{14} \text{ g s}^{-1} \text{ yr}^{-1}$  for a sudden reversal and  $d\dot{M}/dt = -2 \times 10^{15} \text{ g s}^{-1} \text{ yr}^{-1}$  for a smooth transition
- GX 1+4:  $d\dot{M}/dt = 1.3 \times 10^{17} \text{ g s}^{-1} \text{ yr}^{-1}$  for a sudden reversal and  $d\dot{M}/dt = 1.8 \times 10^{17} \text{ g s}^{-1} \text{ yr}^{-1}$  for a smooth transition
- OAO 1657-415:  $d\dot{M}/dt = -1.2 \times 10^{17} \text{ g s}^{-1} \text{ yr}^{-1}$  for a sudden reversal and  $d\dot{M}/dt = -5 \times 10^{17} \text{ g s}^{-1} \text{ yr}^{-1}$  for a smooth transition

In Figure 4.3, two possibilities for this time variability within the PBS model are shown. In Figure 4.3a the mass supplied from the donor star was increased by a total  $\Delta\dot{M}_* = 1.47 \times 10^{16} \text{ g s}^{-1}$  from about  $2.00 \times 10^{16} \text{ g s}^{-1}$  to  $3.47 \times 10^{16} \text{ g s}^{-1}$  over the computed 400 yr time period, corresponding to  $d\dot{M}/dt = 3.68 \times 10^{13} \text{ g s}^{-1} \text{ yr}^{-1}$ , which lead to a long-term spin-up of the NS. The overall luminosity variability changes only very slightly with time, as does the shape of the short-term spin-up/spin-down reversals. The opposite case, a decreasing  $\dot{M}_*$  by a total of  $\Delta\dot{M}_* = -8.47 \times 10^{15} \text{ g s}^{-1}$  from about  $2.00 \times 10^{16} \text{ g s}^{-1}$  to  $1.15 \times 10^{16} \text{ g s}^{-1}$  during the 400 yr period, corresponding to  $d\dot{M}/dt = -2.12 \times 10^{13} \text{ g s}^{-1} \text{ yr}^{-1}$ , can be seen in Figure 4.3b, where a long-term spin-down is superposed over the short-term spin-up/spin-down variability.

These mass loss rate changes  $d\dot{M}/dt$  are one to four orders of magnitude smaller compared to those used in the Yi et al. (1997a,b) model. It should, however, be noted that the above shown long-term trends are only a qualitative example of how a long-term spin-up or spin-down trend superposed on short-term reversals can be achieved with the PBS model. For an application to individual systems, this parameter can be adjusted as needed and thus might also constrain the change of mass loss rate of the companion.

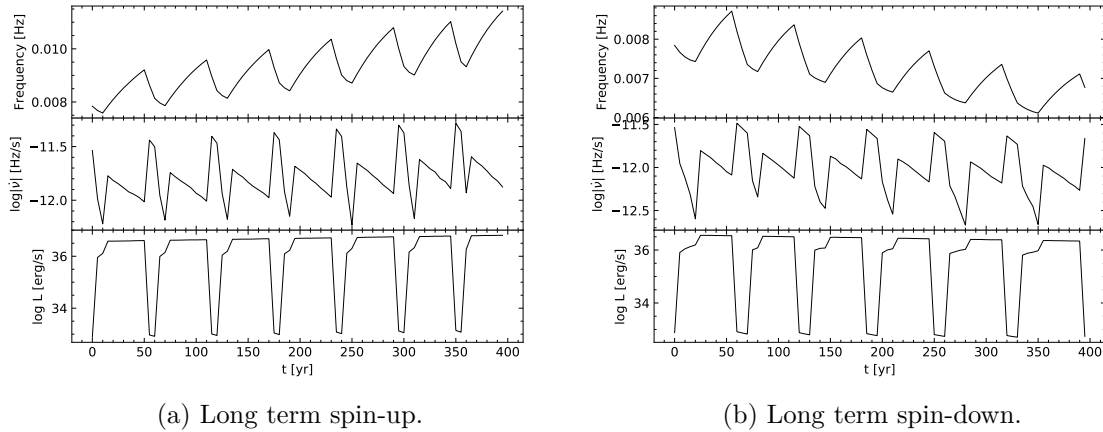


Figure 4.3: A time variable mass supply from the companion star ( $\dot{M}_*$ ) can produce long term spin-up or spin-down of a system, superposed on short term spin reversals. The system parameters in this example are  $B = 6 \times 10^{13}$  G,  $\chi = 45^\circ$ ,  $\beta = 0.3$ ,  $\nu = 8$  mHz.

### 4.3 The Spin-Period Evolution of OAO 1657-415

The pulse period history of pulsar OAO 1657-415 can be seen in Figure 2.5 where a sinusoidal function with a period of roughly 5 yr was superposed on a long-term linear spin-up trend. This sinusoidal behavior shows the spin-up/spin-down reversals with a peak-to-peak amplitude of  $\Delta\nu \approx 0.25$  mHz and the observed luminosity fluctuations (see e.g. Jenke et al. 2012) are within an order of magnitude.

To investigate whether these features are reproducible with the PBS model, several hundred numerical calculations were performed, varying the parameters  $B$ ,  $\chi$  and  $\beta$ . The mass of the NS was assumed to be  $1.74 M_\odot$  with a radius of 10 km, the initial frequency was set to  $\nu \approx 26.95$  mHz, and the mass accretion rate  $\dot{M}_* \approx 3.98 \times 10^{17} \text{ g s}^{-1}$ . The first 30 yr were calculated with a resolution of 0.5 yr.

The focus was to reproduce the short-term spin-up/spin-down trend on a timescale of  $\sim 5$  yr. To achieve this result, the magnetic field was anticipated to be high, as explained in the previous Section. Therefore the first iteration included a magnetic field range of  $B = 1 \times 10^{12}$  G to  $1 \times 10^{15}$  G, the inclination angle was varied between  $\chi = 15^\circ$  to  $85^\circ$  and  $\beta$  was assumed to be 0.3. After examination of the results, the following iterations were chosen with adjusted and narrower ranges. For example, inclination angles below  $\chi = 30^\circ$  did not yield any periodic solution and were discarded and magnetic fields below  $B = 1 \times 10^{13}$  G did not show the desired 5 yr torque reversal timescale. The elasticity parameter was also varied in several iterations between 0.3 and 1.0. After repeating this process numerous times, the magnetic field was limited between  $6 \times 10^{13}$  G to  $7 \times 10^{14}$  G, the inclination angle between  $34^\circ$  to  $40^\circ$  and beta was set to 0.8.

In Figure 4.4 the thus achieved currently best result for OAO 1657-415 is shown. The time variability on a timescale of roughly 5 yr was realized with a magnetic field of  $7 \times 10^{13}$  G, an inclination angle of  $36^\circ$  and an elasticity parameter of  $\beta = 0.8$ . With this solution, however, the amplitude of the frequency variations is with  $\Delta\nu \approx 2.1$  mHz almost ten times larger than the  $\Delta\nu \approx 0.25$  mHz that can be seen in Figure 2.5. Also,



the luminosity spans over four orders of magnitude during each spin-up/spin-down cycle, which does not match the observations. An additional component including a constant luminosity, for example from the X-rays produced by accretion from the stellar wind, might explain this discrepancy as it would level the amplitude of the luminosity variations out.

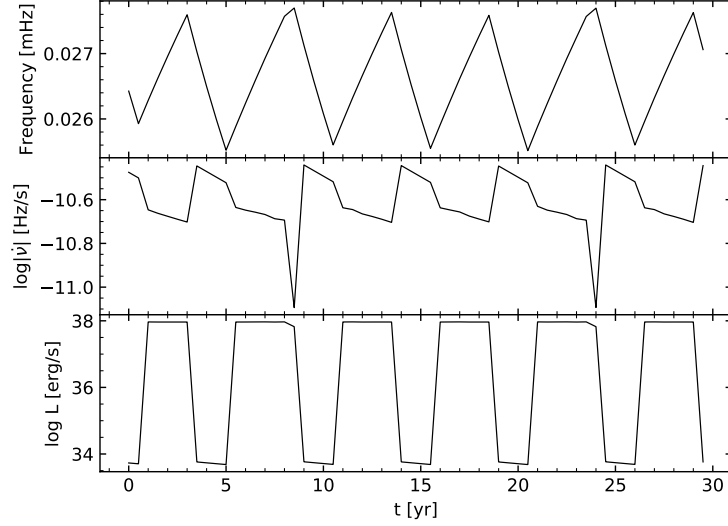


Figure 4.4: A possible solution for OAO 1657-415. The parameters are  $B = 7 \times 10^{13}$  G,  $\chi = 36^\circ$  and  $\beta = 0.8$ .

A peculiar feature can be seen in the middle panel of Figure 4.4. The frequency drops to a minimum and “spikes” in only 1/3 of the cases. If this is an actual physical effect or caused by the calculation, for example due to poor time resolution, is not yet clear.

The magnetic field strengths of accreting pulsars are typically determined either from the cyclotron resonant scattering feature (see Section 5.2.4 for a brief introduction) or by applying accretion torque models. The determined magnetic fields from the cyclotron resonant feature are typically of order  $10^{12}$  G (Staubert et al. 2019; Taani et al. 2018). The magnetic field strengths calculated from accretion torque models on the other hand show a wider range from about  $6 \times 10^{11}$  G to  $8 \times 10^{14}$  G (Staubert et al. 2019). This discrepancy could not yet be explained. The determined magnetic field of the pulsar in OAO 1657-415 of  $B = 7 \times 10^{13}$  G is therefore comparably high, but still feasible.



# Torque-Flux Correlation of OAO 1657-415

This chapter examines the torque-flux correlation of the pulsar in OAO 1657-415. This correlation can be used to gain a deeper understanding of the accretion processes present in this particular source, as well as constrain its magnetic field strength and distance.

A correlation between torque and flux is expected in accreting pulsars when an accretion disk is present. Jenke et al. (2012) studied the pulsar in OAO 1657-415 using data from the Gamma-Ray Burst Monitor (GBM) onboard the Fermi Gamma-Ray Space Telescope (hereafter referred to as *Fermi*/GBM) and the Burst Alert Telescope (BAT) onboard the Neil Gehrels Swift Observatory (hereafter *Swift*/BAT). The frequency history, as well as the frequency derivative ( $\dot{\nu}$ ) and measured BAT flux between MJD 54700 and 55900 can be seen in Figure 5.1 (Jenke et al. 2012).

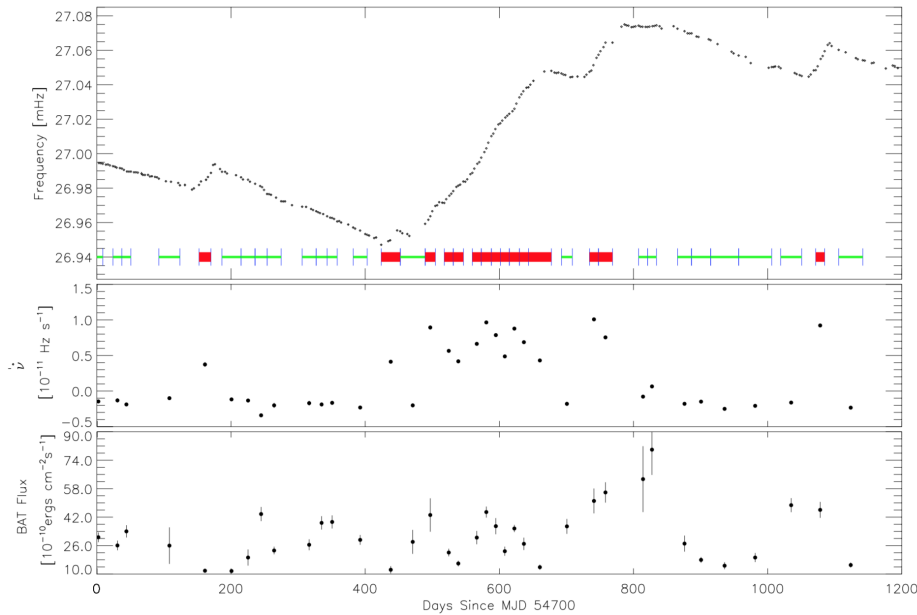


Figure 5.1: Frequency history (top panel), frequency derivative  $\dot{\nu}$  (middle panel) and BAT flux (bottom panel). The intervals during which  $\dot{\nu}$  was determined are indicated at the bottom of the top panel. The intervals where a positive correlation between  $\dot{\nu}$  and flux was found are indicated in red (Jenke et al. 2012).

To study the torque-flux relation, the measured BAT flux was plotted against the calculated frequency derivative ( $\dot{\nu}$ ) and can be seen in Figure 5.2. Jenke et al. (2012) then fit the data with  $\dot{\nu} > 3 \times 10^{-12} \text{ Hz s}^{-1}$  with a model  $\dot{\nu} \propto F^{6/7}$ . These results

suggest that during the spin-up phases a stable accretion disk is present. An anti-correlation between spin-down and flux, which would indicate the presence of a retro-grade accretion disk, was not found (Jenke et al. 2012).

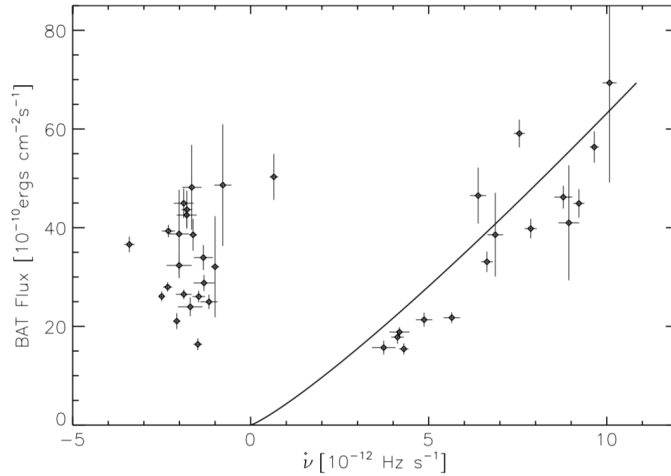


Figure 5.2: *Swift*/BAT flux plotted against  $\dot{\nu}$  of OAO 1657-415. A model with  $\dot{\nu} \propto F^{6/7}$  was used for the fit where  $\dot{\nu} > 3 \times 10^{-12} \text{ Hz s}^{-1}$  (Jenke et al. 2012).

Since the results of Jenke et al. (2012) were published, about 7 years of data was gathered by *Fermi*/GBM and *Swift*/BAT. The aim of the present thesis is to analyze this data with a special focus on the torque-flux relation. In the following Section 5.1, a brief introduction to the satellites and instruments from which the data is taken is given, as well as a description of its processing and filtering. In Section 5.2 the torque-flux relation is studied, the correlation determined and the magnetic field and distance to OAO 1657-415 is calculated using different accretion-torque models.

## 5.1 Data Processing

For the analysis of the torque-flux relation of the pulsar in OAO 1657-415, data spanning from MJD 54694 to 58460 (August 16, 2008 - December 8, 2018) from *Fermi*/GBM and *Swift*/BAT was used. In the following, both satellites and instruments will be briefly introduced and the processing and filtering of the data described. The technical information for *Fermi*/GBM and *Swift*/BAT is based on Meegan et al. (2009) and Krimm et al. (2013) respectively.

### 5.1.1 *Fermi*/GBM

The *Fermi* Gamma-Ray Space Telescope was launched on June 11, 2008. It orbits Earth at an altitude of 565 km and has two instruments on board, the Large Area Telescope (LAT) and the Gamma-Ray Burst Monitor (GBM). The LAT detects gamma-rays above 20 MeV, while the GBM observes at lower energies (8 keV to 40 MeV). The GBM comprises 12 thallium activated sodium iodide (NaI(Tl)) and two bismuth germanate (BGO) scintillation detectors. The direction of the gamma-ray bursts are determined with the NaI(Tl) detectors in the low-energy range from 8 keV to 1 MeV. They are 12.7 cm in diameter and have a thickness of 1.27 cm. With an energy range of 200 keV to 40 MeV, the BGO detectors are overlapping with the NaI(Tl) detectors

at low energies and with the LAT at high energies. The BGOs have a diameter and a length of 12.7 cm. The frequency histories of the sources monitored by the GBM pulsar monitoring team may be found at the GBM pulsar website.<sup>1</sup>

The data for the pulsar in OAO 1657-415 was retrieved from this website. This data was previously reduced and analyzed. It is corrected to the solar system barycenter and for the orbital motion of the pulsar around the companion star using the orbital data from Jenke et al. (2012). Also, no measurements were made during the eclipse.

### Frequency History

In the top panel of Figure 5.3 the frequency measured by *Fermi*/GBM is displayed for the timespan of MJD 54694 to 58460. It is evident that the pulsar is not on a long-term spin-up trend any more, compared to Figure 2.5. Instead, it seems that OAO 1657-415 has reached an equilibrium frequency with smaller spin-up and spin-down phases. The average frequency during this timespan is 27.04 mHz.

### Frequency Derivative ( $\dot{\nu}$ )

In order to calculate the frequency derivative ( $\dot{\nu}$ ) of the *Fermi*/GBM data, time intervals were determined where pulsations were detected and showed a clear trend, i.e. not include a torque reversal. A time interval was also required to be between 11 d to 33 d long and it had to include at least 3 frequency data points. The determined intervals can be also be seen in the top panel of Figure 5.3. The average value of the derivative over the intervals was determined by taking the difference quotient. The results can be seen in the second panel of Figure 5.3.

#### 5.1.2 *Swift*/BAT

The Neil Gehrels *Swift* Observatory's primary task is the swift detection of gamma-ray bursts. This requires a large field of view, a good sensitivity and a sufficient angular resolution for the narrow-field instruments to follow-up on detections. The detectors of BAT onboard *Swift* are made of CdZnTe that are sensitive in the 15 keV to 150 keV energy range. *Swift*/BAT data was used because the flux provided by *Fermi*/GBM has very high uncertainties and low accuracy. Because of its wide field of view, BAT monitors 80% to 90% of the sky daily. Therefore it can provide data taken almost simultaneous to *Fermi*/GBM with only very few gaps. The *Swift*/BAT transient monitor results<sup>2</sup> were provided by the *Swift*/BAT team.

### Rate-to-Flux Conversion Factor

The accretion torque is, according to Equation (3.4), proportional to the whole luminosity in the X-ray energy range, which spans from approximately 0.1 keV to 200 keV. The lightcurve provided by the *Swift*/BAT team, however, spans only from 15 keV to 50 keV. Therefore, by using only the luminosity in the 15 keV to 50 keV energy range, the accretion torque would be underestimated and the conclusions drawn from further calculations might be misleading. Therefore, the *Swift*/BAT flux will be extrapolated

<sup>1</sup><https://gammaray.msfc.nasa.gov/gbm/science/pulsars.html>

<sup>2</sup><https://swift.gsfc.nasa.gov/results/transients/>

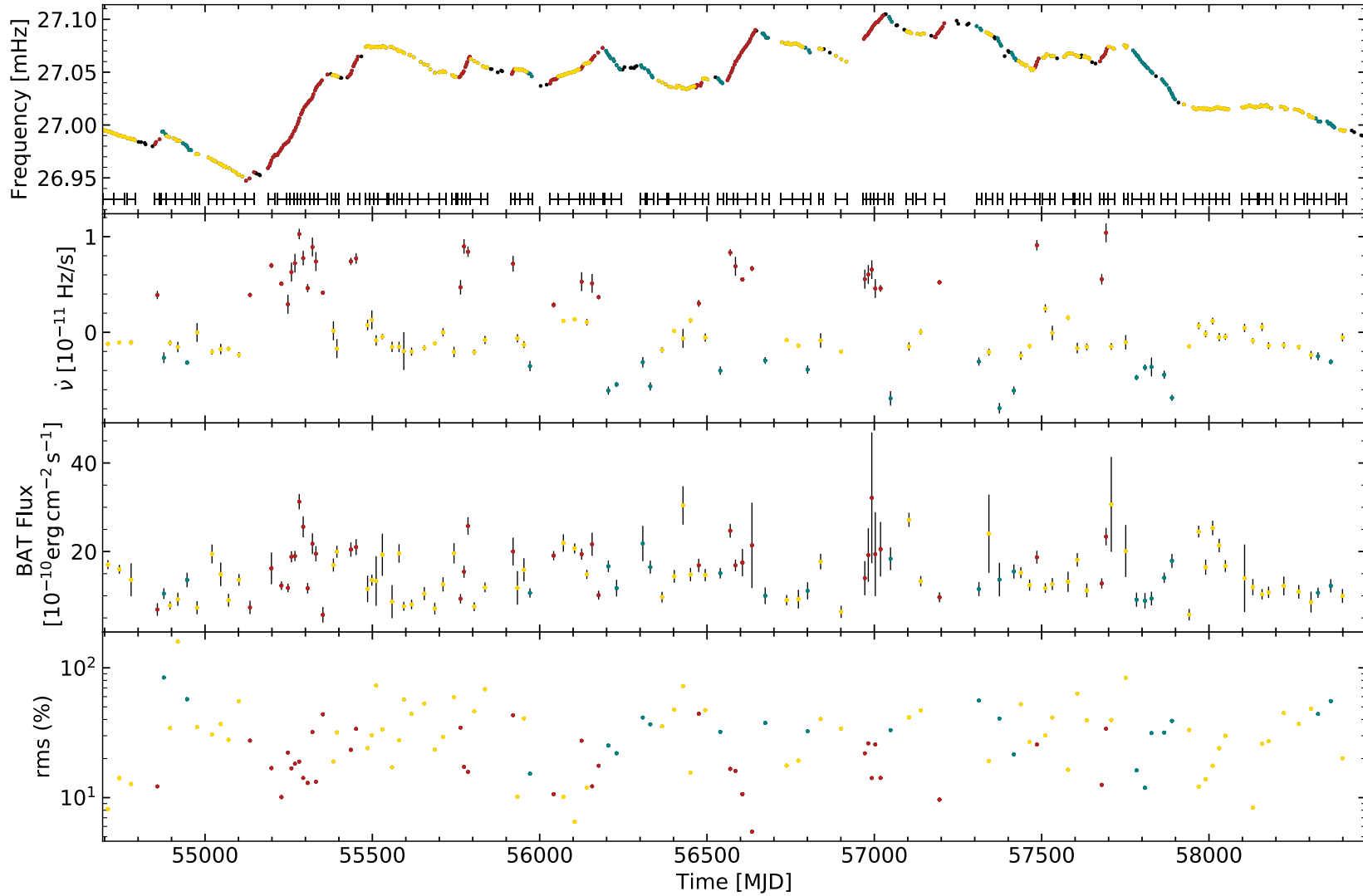


Figure 5.3: Frequency (top panel), frequency derivative ( $\dot{\nu}$ ) (second panel), BAT Flux (third panel) and root mean square (rms) (bottom panel) of OAO 1657-415 from MJD 54694 to 58460. The colors indicate different regions: red designates the spin-up branch where  $\dot{\nu} > 2.5 \times 10^{-12} \text{ Hz s}^{-1}$ , blue-green shows the spin-down branch with  $\dot{\nu} < -2.5 \times 10^{-12} \text{ Hz s}^{-1}$  and yellow points indicate data where  $-2.5 \times 10^{-12} \text{ Hz s}^{-1} < \dot{\nu} < 2.5 \times 10^{-12} \text{ Hz s}^{-1}$ .

to a larger energy range using the XSPEC 12.10<sup>3</sup> software, the information on the spectral shape of OAO 1657-415 from Orlandini et al. (1999) and the response file provided by the *Swift*/BAT team.

The spectral model of OAO 1657-415 from Orlandini et al. (1999) includes low-energy absorption, a power law and a high-energy cutoff.<sup>4</sup> The photo-electric absorption can be calculated via

$$M(E) = \exp(-N_{\text{H}}\sigma(E)), \quad (5.1)$$

with  $\sigma(E)$  the photo-electric cross-section and  $N_{\text{H}}$  is the column density of neutral hydrogen atoms. The power law with high-energy exponential cutoff is

$$A(E) = \begin{cases} K E^{-\alpha} \exp\left(\frac{E_c - E}{E_f}\right), & \text{for } E > E_c \\ K E^{-\alpha}, & \text{for } E \leq E_c \end{cases} \quad (5.2)$$

where  $K$  is a normalization,  $\alpha$  is the power law photon index,  $E_f$  the e-folding energy and  $E_c$  the cutoff energy. The best fit parameters for the combination of photo-electric absorption and power law with high-energy cut-off were taken from Orlandini et al. (1999) and are summarized in Table 5.1. The normalization was assumed to be unity.

Table 5.1: Best fit parameters from Orlandini et al. (1999) for a low-energy absorption, power law and high energy cutoff model for OAO 1657-415.

Model	Parameter	Value
Absorption	$N_{\text{H}}$ [ $10^{22} \text{ cm}^{-2}$ ]	12.7
Power law	$\alpha$	0.83
High-E cutoff	$E_c$ [keV]	13.0
High-E cutoff	$E_f$ [keV]	21.2

The energy flux from 1 keV to 200 keV is  $8.6068 \times 10^{-8} \text{ erg cm}^{-2} \text{ s}^{-1}$  and by comparing this to the *Swift*/BAT rates in the 15 keV to 50 keV range, this returns a conversion factor of  $7.9944 \times 10^{-8} \text{ erg count}^{-1}$ . The measured rates were converted into fluxes using this conversion factor.

## Orbital Phase Diagram

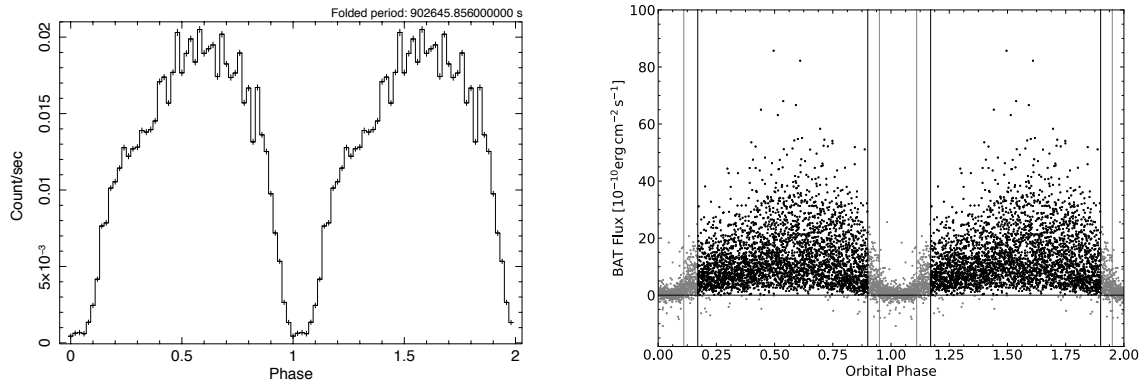
The goal of the data processing is to derive the torque-flux relation of the pulsar in OAO 1657-415. The X-ray luminosity of the pulsar is proportional to the mass accretion rate, see Equation (3.4), and also to the accretion torque. Also, the luminosity can be derived from the observed flux, see Equation (3.5), but in order to calculate the actual luminosity of the pulsar, the flux observed during the eclipse must be removed as described in the following.

The orbital phase of the system can be determined from the orbital period,  $P_{\text{orb}}$ ,

$$P_{\text{phase}}(T) = \frac{T - T_0}{P_{\text{orb}}} - \text{int}\left(\frac{T - T_0}{P_{\text{orb}}}\right), \quad (5.3)$$

<sup>3</sup>Goddard Space Flight Center; Arnaud K. A., Dorman B., Gordon C., HEASARC Software Development.

<sup>4</sup>In XSPEC: phabs\*po\*highcut.



(a) Folded orbital phase diagram of OAO 1657-415, using an orbital period of 10.447 29 d (Jenke et al. 2012). (b) Orbital phase diagram of OAO 1657-415. The vertical light gray lines correspond to a 16% eclipse of the system, the vertical black lines to a 27% eclipse.

Figure 5.4: Orbital phase diagrams of OAO 1657-415. For clarity, two cycles are displayed back-to-back.

where  $T_0$  is a reference time and “int” denotes the integer part of the resulting float number. Thus, the orbital phase will be a number between 0 and 1, corresponding to the start and end point of a binary orbit. For the pulsar in OAO 1657-415, the orbital period is 10.447 29 d long (Jenke et al. 2012) and the orbital phase was calculated using Equation (5.3). The folded orbital phase diagram can be seen in Figure 5.4a, two cycles are shown for clarity.

Since negative fluxes are unphysical, likely caused by an overestimation of the background, these were removed from the data set. Also, according to Jenke et al. (2012), the eclipse of OAO 1657-415 lasts 16% of the binary orbit of the system. The vertical gray lines in Figure 5.4b correspond to this eclipse. van der Meer et al. (2005) studied the HMXB 4U 1700-37 whose “physical” eclipse should last for about 14% of the orbit ( $\phi = 0.07$ ). Because of absorption by the stellar wind, however, the actual end of the eclipse was determined to be at  $\phi = 0.12$ , corresponding to 24% of the orbit. Since this system is comparable to OAO 1657-415, it is reasonable to assume a similar ratio and therefore the actual eclipse is assumed to last about 27% instead of 16% of the orbit. Thus, the eclipse ingress is at  $\phi = 0.90$  and the egress is at  $\phi = 0.17$ . All measured fluxes during the eclipse were removed from the dataset. In Figure 5.4b, this eclipse is indicated by the vertical black lines and all measured fluxes during the eclipse were removed from the dataset.

In order to relate the *Swift*/BAT fluxes to the frequency derivative ( $\dot{\nu}$ ), the average value of the measured fluxes was calculated for each time interval (see Section 5.1.1 and the top panel of Figure 5.3). These fluxes are displayed in the third panel of Figure 5.3.

### Root Mean Square

The *Swift*/BAT fluxes show different variability at different times. In order to quantify this variability, the root mean square (rms) value was calculated for each time interval (as indicated in the top panel in Figure 5.3). The rms characterizes the variability of a quantity, meaning that it is sensitive to the amplitude variations (Reig 2007). It is



defined as

$$\begin{aligned}
 \text{rms} &= \sigma^2 / \bar{x}^2 \\
 &= \frac{\sigma_{\text{obs}}^2 - \sigma_{\text{exp}}^2}{\bar{x}^2} \\
 &= \frac{\sum_i (x_i - \bar{x})^2 - \sum_i \sigma_i^2}{N \bar{x}^2},
 \end{aligned} \tag{5.4}$$

where  $\bar{x}$  is the average count rate,  $\sigma_{\text{obs}}$  and  $\sigma_{\text{exp}}$  are the observed and expected variances respectively,  $\sigma_i$  are the experimental errors and  $N$  the number of points. The rms is plotted in the bottom panel of Figure 5.3.

## 5.2 Torque-Flux Correlation

After the data was processed and filtered, the torque-flux relation of the pulsar in OAO 1657-415 was plotted in the top panel of Figure 5.5. Since the data seemed to divide into three qualitatively different areas, they were divided into the following domains: a spin-up branch with  $\dot{\nu} > 2.5 \times 10^{-12} \text{ Hz s}^{-1}$ , a spin-down branch with  $\dot{\nu} < -2.5 \times 10^{-12} \text{ Hz s}^{-1}$ , and the area in-between these two branches  $-2.5 \times 10^{-12} \text{ Hz s}^{-1} < \dot{\nu} < 2.5 \times 10^{-12} \text{ Hz s}^{-1}$ .

The latter domain, indicated by the yellow points in the Figure, shows points with low torque  $|\dot{\nu}|$ , which appears to favor negative values, and highly scattered fluxes. In this region, matter might be accreted directly from the stellar wind, explaining the high variability. Another explanation could be provided by the Ghosh & Lamb (1979b) model. In their model, there are essentially two torques present, the inner torque  $N_{\text{in}}$ , that is communicated to the star by the magnetic field lines threading the inner transition zone, and  $N_{\text{out}}$ , communicated by the field lines in the outer transition zone (see also Figure 3.1). The inner torque  $N_{\text{in}}$  is always positive, while the outer torque  $N_{\text{out}}$  can be positive or negative. For slow rotators,  $N_{\text{out}}$  adds an additional spin-up torque on the star, so the net torque  $|N|$  will be large. For fast rotators, on the other hand,  $N_{\text{out}}$  contributes a spin-down torque, which will cancel  $N_{\text{in}}$  either partially or completely. Thus, a net spin-down torque might act on the star. The absolute value of the total spin-down torque  $|N|$  will then, however, be smaller compared to the net spin-up torque in the slow rotator limit. This would explain the observed distribution of the data-points. During spin-down, the magnitude of the torque, here denoted by  $|\dot{\nu}|$ , is smaller compared to the spin-up, where  $|\dot{\nu}|$  reaches larger values.

### 5.2.1 Correlation Coefficient and Probability

In the following, only values  $\dot{\nu} > 2.5 \times 10^{-12} \text{ Hz s}^{-1}$  on the spin-up branch and for symmetry  $\dot{\nu} < -2.5 \times 10^{-12} \text{ Hz s}^{-1}$  in the spin-down domain were considered, indicated by the red and blue-green points in the Figure respectively. In these regions of the plot, the points seem to show a correlation. To quantify the significance of this correlation and anti-correlation, the Pearson correlation coefficient and the null hypothesis probability were calculated, see Taylor (1997). The correlation coefficient,  $r$ , is defined as

$$r = \frac{\sum (x_i - \bar{x})(y_i - \bar{y})}{\sqrt{\sum (x_i - \bar{x})^2 \sum (y_i - \bar{y})^2}}, \tag{5.5}$$

where values close to  $\pm 1$  indicate a good linear correlation, and values close to 0 mean little or no correlation. According to Taylor (1997), the null hypothesis probability is calculated using

$$\text{Prob}_N(|r| \geq |r_0|) = \frac{2\Gamma((N-1)/2)}{\sqrt{\pi}2\Gamma((N-2)/2)} \int_{|r_0|}^1 (1-r^2)^{(N-4)/2} dr, \quad (5.6)$$

where  $N$  is the number of measurements. Thus, a small value of  $\text{Prob}_N$  indicates a high probability of correlation. If  $\text{Prob}_N(|r| \geq |r_0|) \leq 5\%$  the correlation is called *significant* and a  $\text{Prob}_N(|r| \geq |r_0|) \leq 1\%$  is called *highly significant* (Taylor 1997). The results of the correlation coefficient and corresponding probabilities are shown in Table 5.2.

Table 5.2: Correlation coefficient  $r_0$  and the corresponding probability (Prob) for the examined values of  $\dot{\nu}$  and number of points  $N$ .

$\dot{\nu} [10^{-12} \text{ Hz s}^{-1}]$	$N$	$r_0$	Prob [%]
$> 2.5$	37	0.61	0.007
$< -2.5$	21	-0.48	2.665

Thus, the probability that 37 measurements of two uncorrelated variables yielding  $|r| \geq 0.61$  is 0.007%, and therefore there is *highly significant* evidence of a linear correlation in the spin-up region. In the spin-down region, 21 data-points were below  $\dot{\nu} = -2.5 \times 10^{-12} \text{ Hz s}^{-1}$  and the probability that two uncorrelated variables would result in  $|r| \geq 0.48$  is 2.7%, which means that the correlation is considered *significant*.

Assuming the three-sigma threshold commonly used in particle- and astrophysics, a probability of less than 0.3% is considered significant. With this threshold, the spin-up branch shows a clearly significant correlation, while the spin-down branch does not meet this criterion. More data will be required to draw definitive conclusions.

### 5.2.2 Applying Accretion-Torque Models

Since the data on the spin-up branch with  $\dot{\nu} > 2.5 \times 10^{-12} \text{ Hz s}^{-1}$  shows a clear correlation, it was fit with Equation (3.12) to determine if matter might be accreted from an accretion disk in the slow rotator limit (see Section 3.2.1). Therefore, the function

$$\dot{\nu} = C_1 \cdot F^{6/7} \quad (5.7)$$

was fitted<sup>5</sup> to the data, where  $C_1$  is a constant. The fit can be seen in Figure 5.5.

The so-called  $\chi^2$  test is a measure of the goodness of a fit. The parameter  $\chi^2$  is a sum of squares, in its general form

$$\chi^2 = \sum_1^N \left( \frac{\text{observed value} - \text{expected value}}{\text{uncertainty of observed value}} \right)^2, \quad (5.8)$$

where  $N$  is the number of measurements (Taylor 1997). For a good fit,  $\chi^2$  will be of order  $N$ , otherwise it will be much greater. The best fit will therefore correspond

<sup>5</sup>The fit was performed in python using the `scipy.odr` function. The Orthogonal Distance Regression (ODR) method was applied in this case in order to include the errors of both  $\dot{\nu}$  and the measured flux.

to the minimum  $\chi^2$ . An alternative measure of the goodness of fit is the reduced chi-squared statistic,  $\chi_\nu^2$ , which is the chi-squared per degree of freedom  $\nu$ . According to Taylor (1997), a reduced chi-square  $\chi_\nu^2 \lesssim 1$  indicates that the agreement between data and fit is satisfactory.

For the spin-up branch, the fitting constant  $C_1$  was thus determined to be  $0.388 \pm 0.017$ , where the uncertainty is at  $1\sigma$  confidence level, with a reduced chi-square  $\chi_\nu^2$  of 0.894. The residuals of the fit are displayed in the second panel of Figure 5.5. There appears to be a slight downward trend of the residuals with increasing  $\dot{\nu}$ , indicating that the model of  $\dot{\nu} \propto F^{6/7}$  may not be ideal.

In order to determine if matter may be accreted from a retrograde disk on the spin-down branch, the same model with  $\dot{\nu} \propto F^{6/7}$  was fitted for  $\dot{\nu} < -2.5 \times 10^{-12} \text{ Hz s}^{-1}$ . The constant was determined to be  $0.326 \pm 0.022$  with a  $\chi_\nu^2$  of 0.079, indicating a good fit. The fit and corresponding residuals can also be seen in Figure 5.5. The opposite trend in the residuals can be seen compared to the spin-up branch. With decreasing  $\dot{\nu}$  the residuals appear to decrease.

The determined values for both the spin-up and spin-down regions are summarized in Table 5.3. The trends in the residuals in both spin-up and spin-down regions indicate that the model might not provide the best fit and a different model needs to be used instead. To explore this further, the data both on the spin-up and spin-down branch were fitted with a more general function

$$\dot{\nu} = C_2 \cdot F^D \quad (5.9)$$

and the constants  $C_2$  and  $D$  were determined. The resulting fit can be seen in the top panel of Figure 5.6 and the corresponding residuals are displayed in the bottom panel. Table 5.3 shows the resulting values of  $C_2$  and  $D$ . Especially on the spin-up branch the residuals now seem to show less of a trend, indicating that this might be a better model to fit the data. On the spin-down branch the trend is also less steep, as reflected by the smaller  $\chi_\nu^2$  value that can be found, along with the determined fit parameters, in Table 5.3.

Table 5.3: Determined values for the constant  $C_1$  from the fit  $\dot{\nu} = C_1 \cdot F^{6/7}$  with the standard error at  $1\sigma$  confidence level and residual variance in the first column and corresponding values for the fit with  $\dot{\nu} = C_2 \cdot F^D$  in the second column.

$\dot{\nu} [10^{-12} \text{ Hz s}^{-1}]$	$C_1$	$\chi_\nu^2$	$C_2$	$D$	$\chi_\nu^2$
$> 2.5$	$0.388 \pm 0.017$	0.894	$0.651 \pm 0.085$	$1.232 \pm 0.242$	0.197
$< -2.5$	$0.326 \pm 0.022$	0.079	$0.671 \pm 0.136$	$1.145 \pm 0.355$	0.051

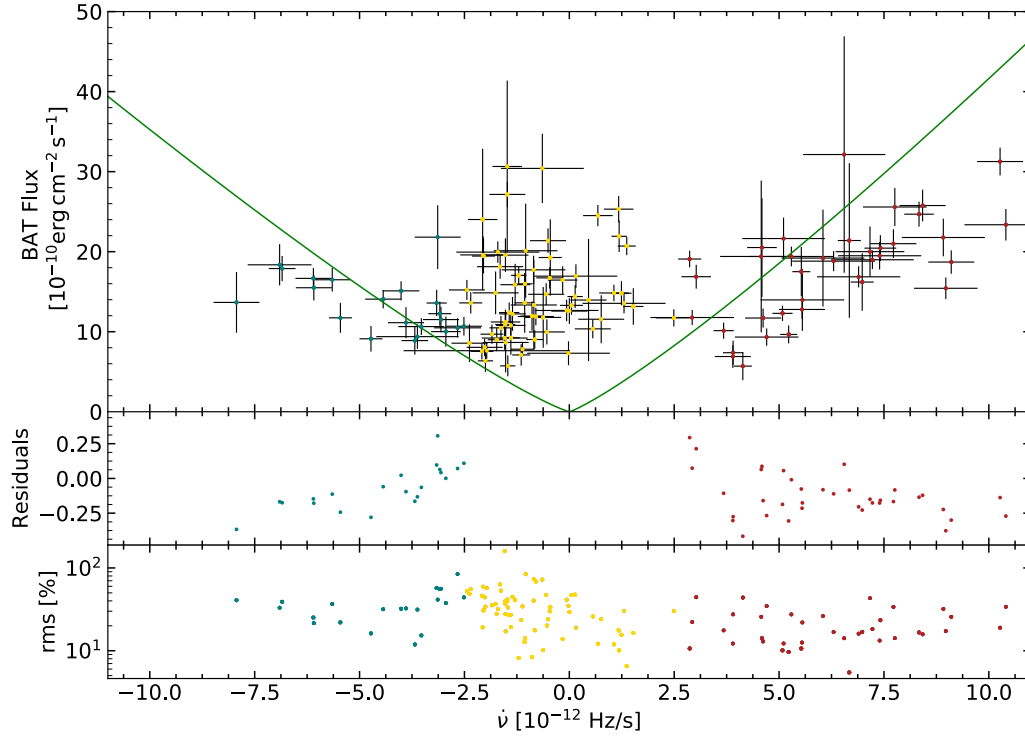


Figure 5.5: Top panel: BAT flux over frequency derivative ( $\dot{\nu}$ ) of OAO 1657-415. The green curves are a fit to the data with  $\dot{\nu} \propto F^{6/7}$  for spin-down smaller than  $-2.5 \times 10^{-12} \text{ Hz s}^{-1}$  and spin-up greater than  $2.5 \times 10^{-12} \text{ Hz s}^{-1}$ . Middle panel: Residuals of the fit. Bottom panel: root mean square (rms) values. The colors in all panels indicate the different regions: red designates the spin-up branch where  $\dot{\nu} > 2.5 \times 10^{-12} \text{ Hz s}^{-1}$ , blue-green shows the spin-down branch with  $\dot{\nu} < -2.5 \times 10^{-12} \text{ Hz s}^{-1}$  and yellow points indicate data where  $-2.5 \times 10^{-12} \text{ Hz s}^{-1} < \dot{\nu} < 2.5 \times 10^{-12} \text{ Hz s}^{-1}$ . The colors are the same as in Figure 5.3.

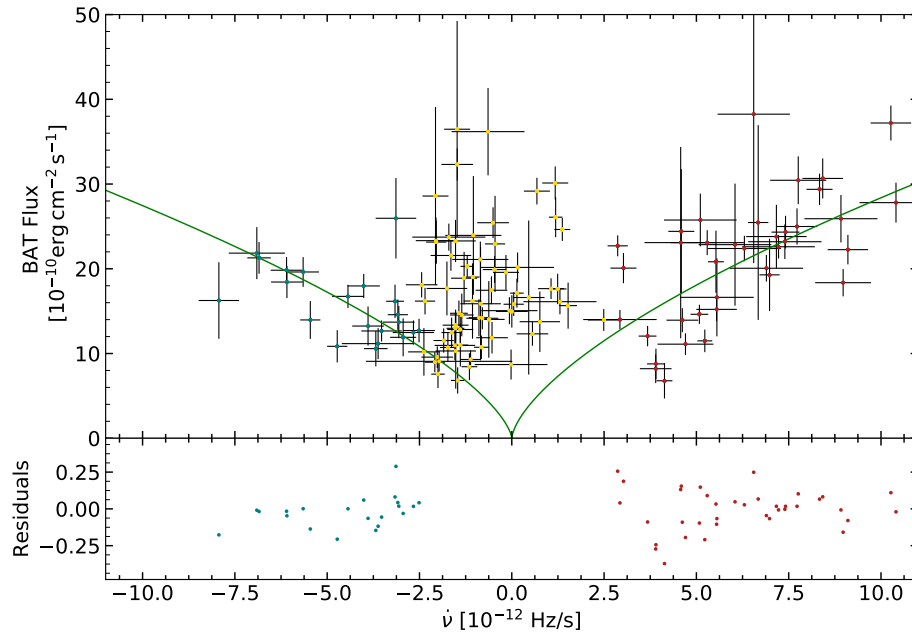


Figure 5.6: Top panel: BAT flux over frequency derivative ( $\dot{\nu}$ ) of OAO 1657-415. The green curves are a fit to the data with  $\dot{\nu} \propto F^D$  (where  $D$  is a constant to be determined) for spin-down smaller than  $-2.5 \times 10^{-12} \text{ Hz s}^{-1}$  and spin-up greater than  $2.5 \times 10^{-12} \text{ Hz s}^{-1}$ . Bottom panel: Residuals of the fit. The colors are the same as in Figures 5.5 and 5.3.

## Root Mean Square

The root mean square (rms) was introduced in Section 5.1.2 as an indicator for the variability of the source during the time intervals indicated in the top panel of Figure 5.3. This rms value was also plotted in the bottom panel of Figure 5.5 and a difference in variability can be seen when comparing the three regions

- $\dot{\nu} < -2.5 \times 10^{-12} \text{ Hz s}^{-1}$  shows an average rms value of  $(36.5 \pm 7.4)\%$ ,
- $\dot{\nu} > 2.5 \times 10^{-12} \text{ Hz s}^{-1}$  has an average rms of  $(20.9 \pm 3.3)\%$ , and
- $-2.5 \times 10^{-12} \text{ Hz s}^{-1} < \dot{\nu} < 2.5 \times 10^{-12} \text{ Hz s}^{-1}$  shows an average of  $(34.8 \pm 5.9)\%$ .

The comparatively low variability in the spin-up region ( $\dot{\nu} > 2.5 \times 10^{-12} \text{ Hz s}^{-1}$ ) might indicate the existence of a stable accretion disk. A recent work by Karino et al. (2019) confirms that an accretion disk might form from a wind in OAO 1657-415. Around torque reversals (where  $\dot{\nu} \approx 0 \text{ Hz s}^{-1}$ ), the accretion disk most likely dissipates and matter is accreted sporadically and impetuously. The spin-down region ( $\dot{\nu} < -2.5 \times 10^{-12} \text{ Hz s}^{-1}$ ) shows a high variability, comparable to that near torque reversals. This might indicate that if a retrograde accretion disk forms, this disk might not be stable.

In order to compare the distribution of the rms value for each region, a histogram was created that can be seen in Figure 5.7. To quantify the comparison of the distributions, a Kolmogorov-Smirnov test was performed. In this test, if the K-S statistic is small or correspondingly the p-value is high, then the hypothesis that the distributions of the two samples are the same cannot be rejected. The results are summarized in the following.

- The comparison of the distribution on the spin-up branch ( $\dot{\nu} > 2.5 \times 10^{-12} \text{ Hz s}^{-1}$ , red data in Figure 5.7) and the spin-down branch ( $\dot{\nu} < -2.5 \times 10^{-12} \text{ Hz s}^{-1}$ , blue-green data in Figure 5.7) returns a K-S statistics of 0.525 with a p-value of 0.0007.
- The comparison of the distribution on the spin-up branch and the data with  $-2.5 \times 10^{-12} \text{ Hz s}^{-1} < \dot{\nu} < 2.5 \times 10^{-12} \text{ Hz s}^{-1}$  (yellow data in Figure 5.7) yields a K-S statistics of 0.417 and a p-value of 0.0003.
- The comparison of the distribution on the spin-down branch and the data with  $-2.5 \times 10^{-12} \text{ Hz s}^{-1} < \dot{\nu} < 2.5 \times 10^{-12} \text{ Hz s}^{-1}$  gives a K-S statistics of 0.214 with a p-value of 0.4111.

Therefore, the distributions of the data on the spin-down branch and the data with  $-2.5 \times 10^{-12} \text{ Hz s}^{-1} < \dot{\nu} < 2.5 \times 10^{-12} \text{ Hz s}^{-1}$  show a high p-value, which indicates that this data likely comes from the same distribution. The lowest p-value is with 0.0003 provided by the second case, comparing the distribution of the data on the spin-up branch and the data with  $-2.5 \times 10^{-12} \text{ Hz s}^{-1} < \dot{\nu} < 2.5 \times 10^{-12} \text{ Hz s}^{-1}$ . This indicates that this data is likely from different distributions.

These results confirm the previous finding that there seems to be a different process happening when the pulsar is spinning up, possibly explained by the existence of an accretion disk. The variability in the spin-down region shows a similar distribution as in the region with  $-2.5 \times 10^{-12} \text{ Hz s}^{-1} < \dot{\nu} < 2.5 \times 10^{-12} \text{ Hz s}^{-1}$ .

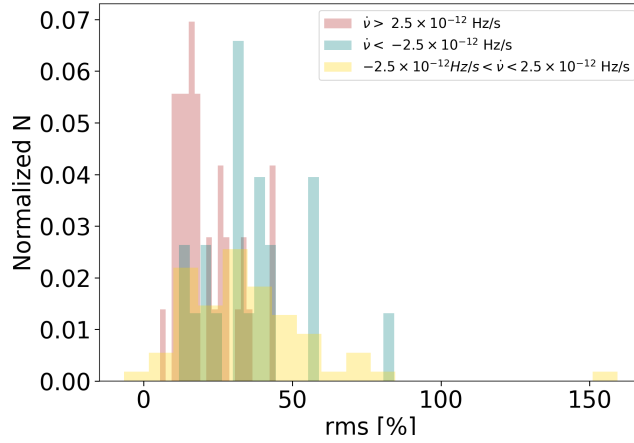


Figure 5.7: Root mean square (rms) histograms for the three regions. The colors are the same as in Figures 5.5 and 5.3.

### 5.2.3 Calculating the Magnetic Field of OAO 1657-415

Since there is strong evidence that an accretion disk is present during the spin-up phases, the following analysis will focus on the region where  $\dot{\nu} > 2.5 \times 10^{-12} \text{ Hz s}^{-1}$ . Different torque-flux models will be further examined in order to estimate the magnetic field and the distance of OAO 1657-415.

In order to calculate the magnetic field of OAO 1657-415, the best fit of the models to the data ( $\dot{\nu}$  and BAT flux) was established using the  $\chi^2$  goodness of fit test explained in Section 5.2.2. Three different models were used together with the measured frequency and flux, an assumed distance of  $d = (7.1 \pm 1.3) \text{ kpc}$  (Audley et al. 2006), a mass of  $M = (1.74 \pm 0.30) M_{\odot}$  (Falanga et al. 2015), a radius of 12 km and a range of magnetic moments. The applied models are:

- Ghosh & Lamb (1979b) find Equation (3.12) for the slow rotator, as described in Section 3.2.1. Therefore, the condition  $\omega_s < 1$  is imposed in the calculation, where  $\omega_s = (r_M/r_{\text{co}})^{3/2}$  is the fastness parameter;
- Wang (1987) improves the Ghosh & Lamb (1979b) model, see Section 3.2.2 and Equations (3.16) - (3.18). Since the system is near equilibrium,  $x_0 = x_{\text{eq}} = 0.971$  is assumed;
- Wang (1995), also explained in Section 3.2.2, reevaluates the toroidal field. Vasilopoulos et al. (2018) applies this model and the torque-flux relation varies only by a normalization factor compared to GL,

$$\dot{\nu} = 30^{-2/7} M^{-10/7} R^{-2/7} n(\omega_s) \xi^{1/2} n_{\text{eff}}^{-6/7} L^{6/7} G^{-3/7} B^{2/7}, \quad (5.10)$$

where  $\xi$  a parameter assumed to be 0.5,  $n_{\text{eff}}$  is the efficiency with which gravitational energy is converted to radiation ( $L_X = n_{\text{eff}} G M \dot{M} / R$ ) and Equation (3.22) is used for  $n(\omega_s)$ . The parameter  $n_{\text{eff}}$  is assumed to be between 0.1 and 1.0 and the condition  $\omega_s < 1$  is imposed.

Each of these models returns an expected value of the frequency derivative  $\dot{\nu}$  and by comparing these to the observed values, a  $\chi^2$  test could be performed. With this

method, the best fit for each model was determined and yields a magnetic moment and thus a magnetic field strength of OAO 1657-415. The magnetic field was left free to vary in the range between  $10^{10}$  G to  $10^{15}$  G. The fits can be seen in Figure 5.8 (blue-green points) and the determined parameters are summarized in the first column of Table 5.5.

The Ghosh & Lamb (1979b) model, see Figure 5.8a, returns a magnetic field strength of  $2.03 \times 10^{12}$  G, which is in good agreement with the rough range of  $1 \times 10^{12}$  G to  $1 \times 10^{13}$  G determined by Jenke et al. (2012). For better comparison, the various determined magnetic field strengths in literature of OAO 1657-415 can be found in Table 5.4. A magnetic field of  $1.54 \times 10^{12}$  G was calculated with the Wang (1987) model, see Figure 5.8b. Only the model by Wang (1995) returns values that significantly deviate from the expected range. Figure 5.8d shows the results for  $n_{\text{eff}} = 0.5$  and Figure 5.8c for  $n_{\text{eff}} = 1.0$ . The latter fit returns a magnetic field of  $1.9 \times 10^{13}$  G with a  $\chi^2$  of 2961, which is significantly higher than those of the Ghosh & Lamb (1979b) and Wang (1987) results.

To explore the influence of the efficiency parameter on the fit, the magnetic field and  $\chi^2$  values were calculated for a range of  $n_{\text{eff}}$  between 0.1 to 1.0. The results can also be seen in the first column of Table 5.5. The magnetic field ranges from  $2.6 \times 10^{11}$  G to  $1.9 \times 10^{13}$  G and the  $\chi^2$  is increasing with increasing  $n_{\text{eff}}$ . Therefore, it seems unlikely that the result for  $n_{\text{eff}} = 1.0$  is reliable. Further discussion will follow in Section 5.2.5.

Table 5.4: Magnetic field strength ( $B$ ) of OAO 1657-415 as determined by different works.

$B$ [ $10^{12}$ G]	Reference
3.1	Orlandini et al. (1999)
10	Yi et al. (1997a,b) (smooth)
5	Yi et al. (1997a,b) (sudden)
20	Yi & Wheeler (1998)
1 to 10	Jenke et al. (2012)
4	Taani et al. (2018)

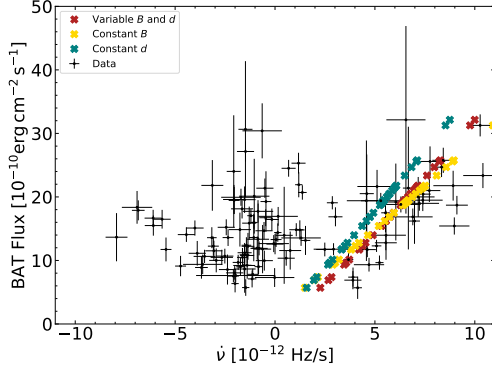
## 5.2.4 Distance Determination

In order to determine the distance to OAO 1657-415, a magnetic field strength has to be assumed in the models of Ghosh & Lamb (1979b); Wang (1987, 1995). In the following, the so-called cyclotron resonance feature will be briefly introduced, as this is the only direct measure of the magnetic field in a pulsar.

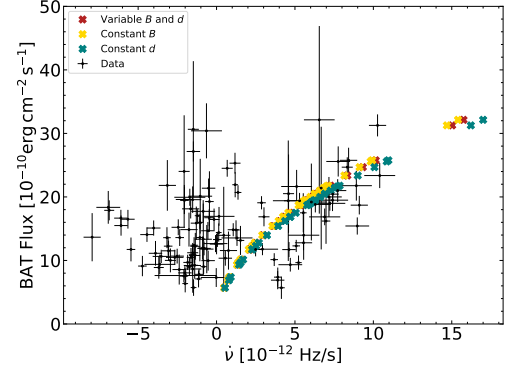
The spectra of accreting NSs show absorption lines at energies in the keV range (see Revnivtsev & Mereghetti 2015). These features are due to cyclotron resonant scattering of radiation by electrons in strong magnetic fields. The motion of the electron perpendicular to the magnetic field lines is quantized in the so-called Landau energy levels (Mészáros 1992). The energy separation between the Landau levels in dependence of the magnetic field,  $B$ , is

$$E_{\text{cyc}} = \hbar \frac{eB}{m_e c} = 11.6 B_{12} \text{ keV}. \quad (5.11)$$





(a) The Ghosh &amp; Lamb (1979b) model for the disk-accretion case.



(b) The improved GL model from Wang (1987).

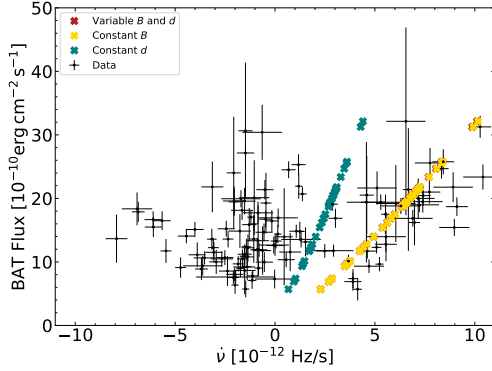
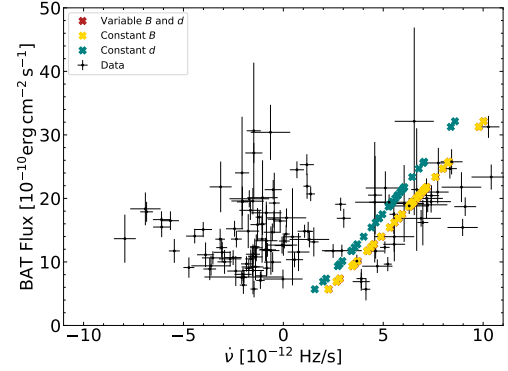
(c) Model by Wang (1995) with  $n_{\text{eff}} = 1.0$ .(d) Model by Wang (1995) with  $n_{\text{eff}} = 0.5$ .

Figure 5.8: Calculating the magnetic field ( $B$ ) and distance ( $d$ ) of OAO 1657-415 using different models of the torque-flux ( $\dot{\nu} - F$ ) relation. The red points (in (b)-(d) partially concealed by the yellow points) show the least  $\chi^2$ -fit for a variable  $B$  and  $d$ . The yellow points show the best  $\chi^2$ -fit for a constant  $B$  and variable  $d$  whereas the blue-green points show the best fit using a constant  $d$  and variable  $B$ . The determined parameters can be found in Table 5.5.

Table 5.5: The distance ( $d$ ), magnetic field ( $B$ ) and corresponding (least)  $\chi^2$  values for the different models: Ghosh & Lamb (1978, 1979a,b) is abbreviated as GL, Wang (1987) indicated as W87 and Wang (1995) as W95 with a range of efficiency parameters ( $n_{\text{eff}}$ ). Columns 2-3 shows the values for a constant  $d = (7.1 \pm 1.3) \text{ kpc}$  (Audley et al. 2006), columns 4-5 for constant  $B = 4 \times 10^{12} \text{ G}$  (Taani et al. 2018) and columns 6-8 show the results where both  $B$  and  $d$  were kept variable.

Model	$d = 7.1 \text{ kpc}$		$B = 4 \times 10^{12} \text{ G}$		$d$ and $B$ var.		
	$B [10^{12} \text{ G}]$	$\chi^2$	$d [\text{kpc}]$	$\chi^2$	$B [10^{12} \text{ G}]$	$d [\text{kpc}]$	$\chi^2$
GL	2.03	866	7.86	814	0.02	15.47	580
W87	1.54	1791	10.84	1757	0.44	3.87	1755
W95, $n_{\text{eff}} = 0.1$	0.26	580	4.58	586	0.01	12.00	580
W95, $n_{\text{eff}} = 0.2$	2.10	582	6.42	584	0.02	15.73	580
W95, $n_{\text{eff}} = 0.3$	7.56	588	7.86	584	0.08	14.95	580
W95, $n_{\text{eff}} = 0.4$	19.18	617	9.16	585	0.13	16.00	580
W95, $n_{\text{eff}} = 0.5$	24.20	846	10.14	584	0.46	14.46	580
W95, $n_{\text{eff}} = 0.6$	24.20	1288	11.22	585	0.66	14.95	580
W95, $n_{\text{eff}} = 0.7$	21.54	1763	12.00	584	0.93	15.21	581
W95, $n_{\text{eff}} = 0.8$	21.54	2209	12.84	584	1.05	16.00	581
W95, $n_{\text{eff}} = 0.9$	19.18	2611	13.51	585	1.48	16.00	581
W95, $n_{\text{eff}} = 1.0$	19.18	2961	14.46	584	2.10	16.00	582

The first cyclotron resonance features in NSs were detected by Trümper et al. (1978) and imply magnetic fields of the order  $10^{12} \text{ G}$  to  $10^{13} \text{ G}$ . A cyclotron line of OAO 1657-415 has been reported (but not yet confirmed) at 36 keV (Orlandini et al. 1999; Staubert et al. 2019), which implies a magnetic field strength of  $B = 3.103 \times 10^{12} \text{ G}$  and a magnetic moment (assuming a NS radius of 12 km) of  $\mu = 5.363 \times 10^{30} \text{ G cm}^3$ . Taani et al. (2018) recently determined the impact of the gravitational redshift  $z$  on the determination of the magnetic field strength of NSs and calculated a magnetic field of  $B = 4 \times 10^{12} \text{ G}$  for OAO 1657-415. By using this magnetic field and corresponding magnetic moment, the same  $\chi^2$  test as discussed above was performed for the different models, now using the distance as the free parameter. The distance was constrained between 3 kpc to 16 kpc (Jenke et al. 2012). The results are also shown in Figure 5.8 (yellow points) and the determined distances are summarized in the second column of Table 5.5.

The distance calculated with the Ghosh & Lamb (1979b) model is 7.86 kpc which is well within the bounds of those determined by other works, for a summary see Table 5.6. Wang (1987) yields a distance of 10.84 kpc, which is further away than the upper bound of Audley et al. (2006), but still within the bounds of Mason et al. (2009); Jenke et al. (2012). Again, the Wang (1995) model determines the most extreme results with 14.46 kpc for  $n_{\text{eff}} = 1.0$ . Table 5.5 also shows the results for a range of  $n_{\text{eff}}$ . The goodness of fit parameter  $\chi^2$  is close to constant but the distance increases monotonically. This is reasonable, as the luminosity and distance are connected through the parameter  $n_{\text{eff}}$ . For a small  $n_{\text{eff}}$ , the luminosity will be correspondingly low and thus the source must be closer. Since the parameter  $n_{\text{eff}}$  is unknown, the distance of the source can only be constrained between 4.58 kpc to 14.46 kpc, which is consistent with the result of Jenke et al. (2012).

Table 5.6: Distance ( $d$ ) to OAO 1657-415 as determined by different works.

$d$ [kpc]	Reference
$> 11$	Chakrabarty et al. (1993)
$6.4 \pm 1.5$	Chakrabarty et al. (2002)
$7.1 \pm 1.3$	Audley et al. (2006)
4.4 to 12	Mason et al. (2009)
3 to 16	Jenke et al. (2012)

### 5.2.5 Simultaneous Calculation of Magnetic Field and Distance

By performing the same  $\chi^2$  fitting method as before but keeping both the distance and the magnetic field as free parameters, the best combination of these variables for a fit of the different models could be found. The results can be seen in Figure 5.8 (red points) and the determined parameters are shown in the last column of Table 5.5.

With this method, the Ghosh & Lamb (1979b) model returns the best fit for a distance of 15.47 kpc and a magnetic field of only  $2 \times 10^{10}$  G. Compared to the results of Sections 5.2.3 and 5.2.4, the distance is now greater while the magnetic field is much lower. The same calculation of the Wang (1987) model returns results closer to those of the literature (see Tables 5.4 and 5.6), that is a distance of 3.87 kpc with a magnetic field strength of  $4.4 \times 10^{11}$  G. Wang (1995) yields a magnetic field strength of  $2.10 \times 10^{12}$  G for  $n_{\text{eff}} = 1.0$  and  $4.6 \times 10^{11}$  G for  $n_{\text{eff}} = 0.5$  with a distance of 16.0 kpc and 14.46 kpc respectively. Since 16.0 kpc is the upper limit of the distance used in the calculation, this solution has to be rejected. Again, a range of  $n_{\text{eff}}$  was studied and the results are also displayed in the last column of Table 5.5. For  $n_{\text{eff}} = 0.4$  and  $n_{\text{eff}} \geq 0.8$  the maximal input distance of 16 kpc yielded the best fit and therefore these results are not meaningful. For the other values of  $n_{\text{eff}}$ , the magnetic field is in the range from  $1 \times 10^{10}$  G to  $9.3 \times 10^{11}$  G and the distance spans from 12.0 kpc to 15.73 kpc.

### Summary of the Magnetic Field and Distance Calculations

The best fit of the Ghosh & Lamb (1979b) model was achieved with a  $\chi^2$  of 580 when both the distance and magnetic field were kept as free parameters. This yielded a distance to OAO 1657-415 of 15.47 kpc and a magnetic field of  $2 \times 10^{10}$  G. The Wang (1987) model returned  $\chi^2$  values that were much higher, owing to the great discrepancy between the data and the fits for large spin-up values, see Figure 5.8b. The best fit for this model, however, was also achieved with a variable distance and magnetic field, returning a distance of 3.87 kpc and a magnetic field of the pulsar in OAO 1657-415 of  $4.4 \times 10^{11}$  G. The Wang (1995) model highly depends on the efficiency parameter. Assuming that at least 50% of the gravitational energy is converted to radiation, the fits with  $n_{\text{eff}} \geq 0.8$  are not meaningful as they assume the highest input value of 16 kpc for a distance to OAO 1657-415. Relevant distances could only be calculated for an efficiency of energy conversion between 50% to 70%, yielding 14.46 kpc to 15.21 kpc with a magnetic field strength between  $4.6 \times 10^{11}$  G to  $9.3 \times 10^{11}$  G. The fits to determine the magnetic field at constant  $d$  get monotonically worse with increasing  $n_{\text{eff}}$ . Only the distance determination at constant  $B$  is meaningful and the  $\chi^2$  values are comparable to those of the Ghosh & Lamb (1979b) fit. Assuming  $n_{\text{eff}} \geq 0.5$ , the distance is between

10.14 kpc to 14.46 kpc.

These distances, ranging in total from 7.86 kpc to 15.21 kpc when omitting the poor fit of Wang (1987), are generally greater than those estimated by Chakrabarty et al. (2002); Audley et al. (2006). Audley et al. (2006) discusses that their result of the distance may be underestimated. Their result depends on the distribution of dust along the line of sight, which was assumed to be uniform. Also, the dust-grain size influences the distance determination,  $d = (7.9 \pm 0.9) a_{0.1}^2$  kpc, where  $a_{0.1}$  is the grain radius in units of  $0.1 \mu\text{m}$ . They found the radius to be  $(0.095 \pm 0.005) \mu\text{m}$ . This is a lot smaller than what Day & Tennant (1991) found for Cen X-3, which is  $(0.34 \pm 0.01) \mu\text{m}$ . Therefore, the distance to OAO 1657-415 may be larger than  $(7.1 \pm 1.3)$  kpc.

The GAIA data release 2 (Gaia Collaboration et al. 2016, 2018) was checked for OAO 1657-415, however, no reliable measurements could be obtained.

The distance determined by Mason et al. (2009) relies on the luminosity by the companion. Since Ofpe/WN9 stars show a large range of luminosities, the distance determination is consequently not well constrained.

Within this discussion, the determined distance range of about 8 kpc to 15 kpc is therefore reasonable but very broad. To further narrow this range, more knowledge of the models with its different parameters is needed, for example how efficient gravitational energy is converted to radiation, as described by the efficiency parameter  $n_{\text{eff}}$ .

The determined magnetic field strengths range from about  $2 \times 10^{10}$  G to  $2 \times 10^{12}$  G, spanning over two orders of magnitude. Due to this wide range, it is not surprising that this includes most of the literature values as can be seen in Table 5.4.

Estimates of the magnetic field strength are highly model-dependent. Therefore, the determination of the magnetic field strength is subject to a lot of uncertainty, as can be deduced from the wide range of magnetic field strengths seen in Table 5.4.

The results of this thesis confirm these findings. The magnetic field strength could only be estimated roughly, it spans from about  $2 \times 10^{10}$  G to  $2 \times 10^{12}$  G, and the results show large differences between the models. As with the distance determination, a more thorough understanding of the models and processes in accreting XRBs is needed to narrow this range.

# Conclusion

In this thesis, the theory on accreting X-ray binaries was studied in the context of accretion-torque models. The basic accretion-torque models were reviewed, including the magnetically threaded disk model developed by Ghosh & Lamb (1978, 1979a,b) and revised by Wang (1987) and Wang (1995), as well as the inclined rotator model presented by Perna et al. (2006). This theory was then applied to the pulsar in OAO 1657-415.

The inclined rotator model by Perna et al. (2006) was first explored in terms of the influence of different parameters to gain a deeper understanding of the model. Thereafter, a time variability of the observable mass supply rate from the companion  $\dot{M}_*$  was introduced to the model in order to achieve a superposition of a long-term spin-up or spin-down trend on short-term spin-up/spin-down reversals. The model was then applied to the pulsar in OAO 1657-415 to estimate its magnetic field strength. A magnetic field of  $7 \times 10^{13}$  G could reproduce the time-scale of variability of approximately 5 yr in this particular source. However, the amplitude of the torque-reversals, as well as the luminosity changes during a cycle deviate significantly from the observed properties of this source. Nonetheless, a magnetic field of  $7 \times 10^{13}$  G is a comparatively high, but still reasonable estimate.

In a second aim of the thesis, the torque-flux correlation of OAO 1657-415 was studied in light of the accretion torque models by Ghosh & Lamb (1978, 1979a,b) and the subsequently revised model by Wang (1987) and Wang (1995). The torque-flux relation was studied in order to determine if matter might be accreted from a prograde or retrograde disk, as well as to estimate the magnetic field strength and distance to OAO 1657-415. Data from *Fermi*/GBM and *Swift*/BAT was used to study the history and torque-flux relation. A first interesting result was that the pulsar seemed to have reached an equilibrium spin frequency of about 27 mHz after a longterm spin-up trend in the past, superposed on smaller spin-up/spin-down reversals.

The torque-flux results showed three different domains, a spin-up branch ( $\dot{\nu} > 2.5 \times 10^{-12} \text{ Hz s}^{-1}$ ), a spin-down branch ( $\dot{\nu} < -2.5 \times 10^{-12} \text{ Hz s}^{-1}$ ) and an intermediate region between these branches. The latter domain with low values of  $|\dot{\nu}|$  displayed a highly scattered flux. The spin-up branch appeared to be correlated, which was quantified using the Pearson correlation coefficient. Strong evidence of correlation was found for this domain, indicating that matter might be accreted from a disk. To determine if a retrograde disk might be present when the NS is spinning down, the spin-down branch was also investigated in terms of an anti-correlation of torque and flux. This branch showed evidence of an anti-correlation but with less statistics compared to the spin-up branch.

The data of the spin-up and spin-down branches were then fit with the Ghosh & Lamb (1979b) model where  $\dot{\nu} \propto F^{6/7}$ . Since the residuals showed a trend, indicating that the model does not fit represent the data, a more general function  $\dot{\nu} \propto F^D$  was fitted with the result that the exponent is closer to about 1.2 instead of 6/7. However,

this exponent could so far not be explained with a model. By studying the root mean square value of the data in the three regions (spin-up and spin-down branches, as well as the data in-between these two), a qualitative difference between the spin-up branch was found compared to the other datapoints. This might further indicate the existence of a stable accretion disk when the NS is spinning up. The observation of a spin-down of the NS with a high flux might be explained through accretion from a retrograde disk (see e.g. Nelson et al. 1997), the data is, however, still inconclusive. Another possibility is that the disk is not behaving entirely Keplerian but instead transitions to sub-Keplerian behavior (see. e.g. Yi et al. 1997a), which could explain the observed properties.

Furthermore, the models by Ghosh & Lamb (1979b); Wang (1987, 1995) were used to constrain the magnetic field and distance to OAO 1657-415. The data were fitted with the different models and one or both of the parameters to be determined were kept free. With a least- $\chi^2$  test, the best fit was determined with the result that the distance to OAO 1657-415 was constrained between approximately 8 kpc to 15 kpc and the magnetic field of its pulsar is likely between about  $2 \times 10^{10}$  G to  $2 \times 10^{12}$  G. These results are in general agreement with other works.

In future studies, the spectral shape or hardness ratio of the data in the three regions (spin-up, spin-down and in-between) could be investigated using different energy bands (e.g. 15 keV to 50 keV and 50 keV to 150 keV) of the *Swift*/BAT satellite in order to determine if different accretion processes are responsible for the observed spin-up and spin-down behavior of the pulsar in OAO 1657-415.

Also, the inclined rotator model of Perna et al. (2006) could be expanded in future work by an additional term that includes the magnetic coupling and thus the toroidal component of the magnetic field in the disk.

---

# Bibliography

---

- Audley, M. D., Nagase, F., Mitsuda, K., Angelini, L., & Kelley, R. L. 2006, MNRAS, 367, 1147
- Barnstedt, J., Staubert, R., Santangelo, A., et al. 2008, A&A, 486, 293
- Basko, M. M. & Sunyaev, R. A. 1976, MNRAS, 175, 395
- Bildsten, L., Chakrabarty, D., Chiu, J., et al. 1997, ApJS, 113, 367
- Bozzo, E., Ascenzi, S., Ducci, L., et al. 2018, A&A, 617, A126
- Bozzo, E., Stella, L., Vietri, M., & Ghosh, P. 2009, A&A, 493, 809
- Bradt, H. 2008, Astrophysics Processes
- Chakrabarty, D., Bildsten, L., Finger, M. H., et al. 1997a, ApJ, 481, L101
- Chakrabarty, D., Bildsten, L., Grunsfeld, J. M., et al. 1997b, ApJ, 474, 414
- Chakrabarty, D., Grunsfeld, J. M., Prince, T. A., et al. 1993, ApJ, 403, L33
- Chakrabarty, D., Wang, Z., Juett, A. M., Lee, J. C., & Roche, P. 2002, ApJ, 573, 789
- Clearbout, J. 1990, Stanford Exploration Project Report, 67, 139
- Day, C. S. R. & Tennant, A. F. 1991, MNRAS, 251, 76
- Falanga, M., Bozzo, E., Lutovinov, A., et al. 2015, A&A, 577, A130
- Forman, W., Jones, C., Cominsky, L., et al. 1978, ApJS, 38, 357
- Fryxell, B. A. & Taam, R. E. 1988, ApJ, 335, 862
- Gaia Collaboration, Brown, A. G. A., Vallenari, A., et al. 2018, A&A, 616, A1
- Gaia Collaboration, Prusti, T., de Bruijne, J. H. J., et al. 2016, A&A, 595, A1
- Ghosh, P. & Lamb, F. K. 1978, ApJ, 223, L83
- Ghosh, P. & Lamb, F. K. 1979a, ApJ, 232, 259
- Ghosh, P. & Lamb, F. K. 1979b, ApJ, 234, 296
- Giacconi, R., Gursky, H., Kellogg, E., Schreier, E., & Tananbaum, H. 1971, ApJ, 167, L67
- Giacconi, R., Murray, S., Gursky, H., et al. 1972, ApJ, 178, 281
- Hanslmeier, A. 2013, Einführung in Astronomie und Astrophysik (German Edition) (Springer Spektrum)
- Jenke, P. A., Finger, M. H., Wilson-Hodge, C. A., & Camero-Arranz, A. 2012, ApJ, 759, 124
- Karino, S., Nakamura, K., & Taani, A. 2019, arXiv e-prints: 1903.03455
- Kretschmar, P. 1996, PhD thesis, Eberhard-Karls-Universität Tübingen
- Krimm, H. A., Holland, S. T., Corbet, R. H. D., et al. 2013, ApJS, 209, 14
- Lewin, W. H. G., Ricker, G. R., & McClintock, J. E. 1971, ApJ, 169, L17
- Longair, M. S. 2011, High Energy Astrophysics
- Maeder, A. & Meynet, G. 1994, A&A, 287, 803
- Makishima, K., Ohashi, T., Sakao, T., et al. 1988, Nature, 333, 746
- Mason, A. B., Clark, J. S., Norton, A. J., et al. 2012, MNRAS, 422, 199
- Mason, A. B., Clark, J. S., Norton, A. J., Negueruela, I., & Roche, P. 2009, A&A, 505, 281

- Matsuda, T., Inoue, M., & Sawada, K. 1987, MNRAS, 226, 785
- Meegan, C., Lichti, G., Bhat, P. N., et al. 2009, ApJ, 702, 791
- Mészáros, P. 1992, High-energy radiation from magnetized neutron stars.
- Nelson, R. W., Bildsten, L., Chakrabarty, D., et al. 1997, ApJ, 488, L117
- Ögelman, H. & van den Heuvel, E. P. J., eds. 1989, NATO Advanced Science Institutes (ASI) Series C, Vol. 262, Timing Neutron Stars
- Orlandini, M., dal Fiume, D., del Sordo, S., et al. 1999, A&A, 349, L9
- Perna, R., Bozzo, E., & Stella, L. 2006, ApJ, 639, 363
- Polidan, R. S., Pollard, G. S. G., Sanford, P. W., & Locke, M. C. 1978, Nature, 275, 296
- Pradhan, P., Maitra, C., Paul, B., Islam, N., & Paul, B. C. 2014, MNRAS, 442, 2691
- Rappaport, S., Markert, T., Li, F. K., et al. 1977, ApJ, 217, L29
- Reig, P. 2007, MNRAS, 377, 867
- Reig, P. 2011, Ap&SS, 332, 1
- Revnivtsev, M. & Mereghetti, S. 2015, Space Sci. Rev., 191, 293
- Rivinius, T. 2013, in Astrophysics and Space Science Proceedings, Vol. 31, Stellar Pulsations: Impact of New Instrumentation and New Insights, ed. J. C. Suárez, R. Garrido, L. A. Balona, & J. Christensen-Dalsgaard, 253
- Seward, F. D. & Charles, P. A. 2010, Exploring the X-ray Universe
- Shapiro, S. L. & Teukolsky, S. A. 1983, Black holes, white dwarfs, and neutron stars: The physics of compact objects
- Staubert, R., Trümper, J., Kendziorra, E., et al. 2019, A&A, 622, A61
- Taani, A., Karino, S., Song, L., Zhang, C., & Chaty, S. 2018, arXiv e-prints: 1808.05345
- Taylor, J. 1997, Introduction to Error Analysis, the Study of Uncertainties in Physical Measurements, 2nd Edition (University Science Books)
- Trümper, J., Pietsch, W., Reppin, C., et al. 1978, ApJ, 219, L105
- Trümper, J. & Schönfelder, V. 1973, A&A, 25, 445
- van der Meer, A., Kaper, L., di Salvo, T., et al. 2005, A&A, 432, 999
- Vasilopoulos, G., Haberl, F., Carpano, S., & Maitra, C. 2018, A&A, 620, L12
- Vietri, M. 2008, Foundations of High-Energy Astrophysics., Theoretical Astrophysics (University of Chicago Press)
- Wang, Y.-M. 1987, A&A, 183, 257
- Wang, Y.-M. 1995, ApJ, 449, L153
- White, N. E. & Pravdo, S. H. 1979, ApJ, 233, L121
- Yi, I. & Wheeler, J. C. 1998, ApJ, 498, 802
- Yi, I., Wheeler, J. C., & Vishniac, E. T. 1997a, ApJ, 481, L51
- Yi, I., Wheeler, J. C., & Vishniac, E. T. 1997b, ApJ, 491, L93



---

# Acknowledgements

---

This thesis would not have been possible without the guidance and help of several individuals. At this point I would like to thank all those who contributed to the success of this bachelor thesis.

I thank Prof. Dott. Andrea Santangelo for his captivating lectures, which accompanied me from the beginning of my physics studies and which reinforced my determination to pursue astrophysics. I thank him for the opportunity to work in his group and offer the topic and supervisor for this thesis. My biggest thanks go to Dr. Lorenzo Ducci, who supervised the work with such great enthusiasm and skill. I thank him for the excellent support, for the open doors and patience for all questions, the thorough proofreading of the thesis and all the fun times we had. I thank my office colleagues, who always had an open ear and offered help, ideas and a great working atmosphere. I thank the IAAT members for welcoming me to the group.

I thank all my friends for supporting and motivating me during my physics studies and my whole life. My deepest thanks go to my family who support me in everything and without whom none of this would have been possible.